Article, Published Version

Ahmari, Alireza; Oumeraci, Hocine

Measurement and Analysis of Wave-Induced Suspended Sediment Transport above Rippled and Plane Seabeds

Die Küste

Zur Verfügung gestellt in Kooperation mit/Provided in Cooperation with:
Kuratorium für Forschung im Küsteningenieurwesen (KFKI)

Verfügbar unter/Available at: https://hdl.handle.net/20.500.11970/101661

Vorgeschlagene Zitierweise/Suggested citation:
Ahmari, Alireza; Oumeraci, Hocine (2011): Measurement and Analysis of Wave-Induced Suspended Sediment Transport above Rippled and Plane Seabeds. In: Die Küste 78. Karlsruhe: Bundesanstalt für Wasserbau. S. 165-234.

Die Küste, 78 (2011), 165-234

Measurement and Analysis of Wave-Induced Suspended Sediment Transport above Rippled and Plane Seabeds

By ALIREZA AHMARI and HOCINE OUMERACI

Zusammenfassung

Sandige Küsten sind ständigen morphologischen Veränderungen unterworfen. Die fortdauernde Küstenverformung und Erosion sind das Ergebnis der Wechselwirkung zwischen Strömung und Sediment, die zu einem Längs- und Quertransport der Sedimente führen. Auf Grund der zunehmenden Besiedlungen und wirtschaftlichen Nutzungen der Küstengebiete (Tourismus, Industrie-Infrastrukturen, Häfen und Mohlen, Offshore-Anlagen, etc.) in den letzten Jahrzehnten werden u.a. verbesserte wissenschaftliche Grundlagen hinsichtlich der Wechselwirkungen zwischen hydro- und morphodynamischen Prozessen zunehmend unverzichtbarer für die Entwicklung verlässlicher prädiktiver Modelle zur Berechnung der Auswirkungen der Ingenieurmaßnahmen auf die küstenmorphologischen Veränderungen. Da die dramatischsten Küstenumformungen infolge des Sedimenttransports unter Sturmflutbedingungen erfolgen, stellt die Suspensionsfracht die wichtigste Transportform der Sedimente durch küstennahe seegangin-duzierte Strömungen dar. Die im Rahmen der vorliegenden Arbeit durchgeführte Wissensstandsanalyse hat dennoch gezeigt, dass trotz zahlreicher Labor- und Feldversuche auf dem Gebiet des Sedimenttransports weder verlässliche Daten noch Modelle vorliegen, die die zeitliche und räumliche Variabilität der Suspensionsfracht sowie die damit verbundenen hydro- und morphodynamischen Prozesse unter den verschiedensten Seegangverhältnissen über geriffelten und glatten Sandsohlen beschreiben können. Aus diesem Grund werden im Rahmen dieser Arbeit umfassende Laboruntersuchungen in dem Großen Wellenkanal (GWK) des Forschungszentrums Küste (FZK), eine gemeinsame zentrale Einrichtung der Leibniz Universität Hannover und der Technischen Universität Braunschweig, mit den folgenden Zielsetzungen durchgeführt: (i) Bestimmung der bestgeeigneten Messtechnik für die Suspensionsfracht anhand einer Vergleichsanalyse der Messdaten ermittelt durch akustische Sensoren (ABS), optische Sensoren (OTM) sowie durch mechanisches System (TSS) unter großmaßstäblichen Laborbedingungen insbesondere über den geriffelten Sandsohlen. (ii) Verbesserung des Wissensstandes der ablaufenden wellen-induzierten Prozesse sowie deren Einfluss auf die Suspensionsfracht und darauf basierend (iii) die Verifizierung des von Nielsen (1979) vorgeschlagenen 1DV Berechnungsmodells, das die zeitliche und räumliche Verteilung suspendierter Sedimentkonzentrationen über geriffelten Sandsohlen unter regelmäßigem und unregelmäßigem Seegang beschreibt.

Schlagwörter

Suspendierter Sedimenttransport, wellen-indizierte Prozesse, Acoustic Backscatter Sensor, ABs, geriffelte Sohle, regelmäßiger Seegang, unregelmäßiger Seegang

Summary

Littoral zones are continuously subject to change as a result of the erosive and accretive relocation of sediment material induced by waves in the nearshore zone. Due to the increasing importance of coastal zones, especially in recent decades, a substantial improvement of our understanding of wave-induced sediment transport mechanisms and morphological processes as well as their interactions with man-made structures is a crucial issue. This particularly applies to an increase in human activ-

ities in the nearshore, onshore and offshore zones (e.g. recreation, infrastructure, harbours and piers, offshore wind turbines). The most dramatic morphological changes and recessions of the coastline generally occur during storms, when the dominant transport mechanism in the nearshore zone is due to suspended load. Nevertheless, a review of present-day knowledge clearly shows that despite the numerous field and laboratory studies on sediment transport, no reliable data and models are yet available which can properly describe the spatial/temporal distribution of suspended sediment concentrations and the associated mechanisms under different wave conditions over a plane or rippled bed. On account of this, it was proposed to carry out extensive laboratory measurements of suspended sediment concentrations, seabed profile evolution and instantaneous wave-induced flow velocity in the Large Wave Flume (GWK) of the Coastal Research Centre (FZK) in Hanover, an institution operated jointly by the universities of Hanover and Brunswick.

Firstly, the most appropriate measuring technique for recording small-scale intrawave sediment entrainment/suspension processes especially above a rippled bed was identified through a comparative analysis of data obtained simultaneously using different measurement techniques, including an Acoustic Backscatter Sensor (ABS), an Optical Turbidity Meter (OTM) and a Transverse Suction System (TSS). Secondly, the data obtained from the most appropriate measuring technique identified (i.e. the ABS) were analysed in order to obtain a better understanding of the intrawave mechanisms governing the entrainment and suspension of sediment above both plane and rippled beds. Thirdly, an integrated approach based on the one-dimensional diffusion equation was developed for modelling intrawave sand transport processes above rippled beds beneath non-breaking waves. The 1DV model proposed by Nielsen (1989) was considered and verified using the most relevant non-dimensional hydrodynamic and morphological parameters derived from the results of Step 2. This model was successfully applied to describe phase-dependent sand entrainment and suspension processes close to a rippled seabed.

Keywords

Suspended sediment transport, intrawave processes, Acoustic Backscatter Sensor, ABS, rippled seabed, plane seabed, non- breaking waves, near-breaking waves

Contents

1. Introduction

The range of applications of models for suspended sediment transport, which constitutes the major part of the total nearshore sediment transport by waves, is continuously increasing. The vertical distribution of suspended sediment concentration is important for several coastal engineering problems, such as the scour around structures, nearshore morphological changes and the recession of coastlines. Several research investigations involving mathematical, laboratory and field studies have so far been carried out to obtain a better description of suspended load. Most of these studies, however, include a number of simplifications and assumptions such as the time-averaged or depth-averaged treatment of suspended sediment concentration characteristics. Although the number of sediment transport models is growing rapidly, many of these models are purely empirical and a generic description of sediment transport is still not available. In order to arrive at more reliable as well as generic models, an integrated consideration of the nearshore hydrodynamic and morphodynamic processes responsible for the spatial and temporal variation of suspended sediment concentration is urgently required. This is particularly the case during storm events over the entire nearshore zone, when wave-induced sediment transport is primarily governed by suspended load. Furthermore, a knowledge of the vertical distribution of suspended sediment concentration is additionally required to calculate the total sediment transport. Owing to the phase difference between the magnitudes of flow velocity and suspended sediment concentration induced by unsteady flow, information is not only required concerning the mean concentration of suspended sediment and the mean flow velocity, but also a de-

tailed description of the temporal and spatial variations of these parameters above different seabed forms. This study more specifically concerns a description of the temporal and spatial entrainment of sediment under different wave conditions in the nearshore zone.

2. State of knowledge regarding measuring and modelling techniques

In order to predict long-term changes in the nearshore zone, particularly under erosive conditions, a detailed analysis of the pertaining hydrodynamic and morphodynamic processes and their interaction is required. A suitable method of carrying out this analysis is to perform a sediment flux calculation. A review of different bed form regimes has shown that above plane seabeds subject to oscillatory flow, instantaneous sand entrainment takes place by turbulent diffusion, while over rippled seabeds, the sediment dynamics in a near-bed layer with a thickness of about 1-2 ripple heights are dominated by coherent periodic vortex structures. In the case of rippled seabeds, it is very important to consider the phase lags between flow velocities and suspended sand concentration caused by lee-wake vortices in the rippled seabed regime. Despite the large number of data sets available on time-averaged concentrations and ripple dimensions, the number of time-dependent and net transport measurements in large-scale experimental facilities is limited. This means that existing transport models, especially research models, are not sufficiently validated by reliable and accurate experimental data (VAN DER WERF, 2006). Moreover, cross-comparisons of operational and research models for sediment transport have shown that the greatest discrepancies and disagreements occur in the case of rippled seabed regimes. In order to predict suspended sediment processes, a detailed knowledge of the most relevant sediment variables is essential. These include, e.g. the size and settling velocity of the sediment particles as well as important morphodynamic parameters such as the vertical distribution of the suspended sediment concentration, the temporal fluctuation of sediment particles under different flow conditions, and the sediment transport rate. Field and laboratory measurements are required in order to obtain this information. Given the wide range of measuring techniques, which have been developed from simple mechanical samplers to more sophisticated optical and acoustic samplers, an important step is to select the most appropriate technique for a particular purpose. In this context, the literature review given in the following focuses on two major aspects:

- Measurement techniques that have been validated by many different experiments over recent years for measuring the time-dependent sediment entrainment induced under different wave conditions.
- Present state of knowledge regarding the available time-averaged and time-dependent models for predicting suspended sediment concentration and the most commonly used measuring techniques for the accurate measurement of suspended sediment concentrations in large-scale laboratory facilities

2.1 Measuring techniques for suspended load

No rigorous mathematical description of the regularities of two-phase flux motion is yet available (KOS'YAN et al., 1995). The importance of the distribution of suspended sediment concentration due to wave action for a variety of coastal engineering problems has thus led to considerable efforts

to reliably record and analyse suspended sediment transport as the major component of the total sediment load due to waves in the nearshore zone. A determination of empirical relationships describing the suspended sediment transport process is therefore not possible without precise measurement methods and devices. The application of reliable methods for measuring suspended sediment concentration fluctuations in order to improve our knowledge of the entrainment process as well as precise observations of temporal and spatial sediment transport mechanisms rank among the most urgent tasks in the coastal zone. There are several methods to determine the suspended sediment concentration in water, which are based on three main principles:

- The pump-sampling method to measure time-averaged sediment concentration.
- Acoustic methods to measure time-dependent sediment concentration fluctuations.
- Optical methods to measure time-dependent sediment concentration fluctuations.

The pump-sampling method is used to measure the mean suspended sediment concentration over time at different levels above the seabed. Using this simple method allows us to collect sediment samples at given locations with different elevations above the seabed without taking account of the temporal fluctuation of suspended sediment particles under different wave conditions. The result of such measurements is the mean concentration of suspended sediment particles over a specific time period at given levels above the seabed. Although the temporal variation of suspended sediment fluctuations cannot be measured by this method, it is possible to evaluate the time-averaged vertical and horizontal profiles of the suspended sediment distribution above the seabed, which can be very useful regarding the calibration of optical and acoustic devices and the verification of time-dependent measurements. Acoustic and optical methods are used to measure the temporal variation of suspended sediment fluctuations under different flow conditions. The main measurement devices used to measure the time-dependent concentration of suspended particles are:

- The Optical Backscatter Sensor (OBS)
- The Optical Turbidity Meter (OTM)
- The Acoustic Backscatter Sensor (ABS)
- The Laser diffraction device (LISST)
- The Acoustic Doppler Current Profiler (ADCP)

Moreover, a number of acoustic and optical sampling methods permit the non-intrusive measurement of sediment concentrations, which represents an important advantage compared to mechanical sampling methods.

2.1.1 Time-averaged measuring techniques (TSS)

Due to the fact that there is no general method based on basic physical principles to perfectly predict suspended sediment transport, it is necessary to record data from a wider variety of conditions. One of the most important methods to study the distribution of suspended sediment concentration under wave and current action in the coastal environment is to collect time-averaged profiles of suspended sediment concentrations by means of mechanical sampling methods (BOSMAN, 1982). In this context, the Transverse Suction System (TSS) serves as a reliable method to measure time-averaged concentrations of suspended sediment at given elevations above the seabed under current and wave action. The results of investigations by BOSMAN et al. (1987) generally show that measurements under two-dimensional unidirectional flow and oscillatory flow conditions are reliable, provid-

ed that the suction intakes are normal (perpendicular) to the oscillatory flow and that the intake velocity is approximately equal to or greater than the flow velocity (for more details, see CRICKMORE and AKED, 1975 and VAN RIJN, 2006).

2.1.2 Time-dependent measuring techniques

The problem with traditional mechanical devices regarding the measurement of sediment concentrations is that this measuring technique is unable to account for the temporal fluctuations of sediment particles in the water column above the seabed. This is due to the group structure of waves, their transformation within the coastal zone and the contribution of phase shifts between sediment entrainment and the oscillatory water flow at different frequencies of the irregular wave spectrum. In this context, an investigation of the temporal-spatial fluctuation and transport of suspended sediment particles based on suspension mechanisms is necessary to determine the phase and amplitude ratios between the Suspended Sediment Concentration (SSC), the Turbulent Kinetic Energy (TKE) and the wave energy losses due to wave-breaking and shear stress in the seabed boundary layer. Such an approach would permit an estimation of the contribution of sediment entrainment and local convection as well as the diffusion and advection of sediment particles to the sediment concentration over the entire water column. In addition, this would assist in the evaluation of the seabed profile evolution and hence to the near-bed flow regime. In the recent years, advanced techniques to measure the spatial-temporal fluctuations of suspended sediment concentrations have been applied in operational instruments. Such developments include:

- The transmission and scattering of light (optical methods)
- Ultra-sound and the scattering of acoustic energy (acoustic methods)
- Gamma radiation (nuclear methods)

The advantage of such instruments is to provide an instantaneous concentration in the form of an analogue/digital signal (no sample handling) and facilitate all forms of offline data handling. These devices do have certain limitations, however. They are found to suffer from occasional instrument instability, and are highly sensitive to turbidity, particle size and air bubbles. Two measurement methods which are more frequently used to measure the temporal-spatial variations of suspended sediment concentration, namely the optical method (Optical Turbidity Meter; OTM) and the multi-frequency Acoustic Backscattering System (ABS), are briefly discussed in the following.

2.1.3 Optical Turbidity Meter (OTM)

The Optical Turbidity Meter (OTM) (Figure 1), developed at the Russian Academy of Sciences, P.P.Shirshov Institute of Oceanology (KOS'YAN et al., 1995; KOS'YAN et al., 2009a, KOS'YAN et al., 2009b), is commonly used for studying the time-dependent distribution of suspended particle concentration and turbidity in the near-bed layer of nearshore zones, where fairly coarse particles of inorganic origin (>50 μm) at high concentrations prevail. The Optical Turbidity Meter (OTM) is a suitable optical device for the selective measurement of the time-dependent fluctuations of suspended sediment concentration at the different heights above the sea bed (point measurements).

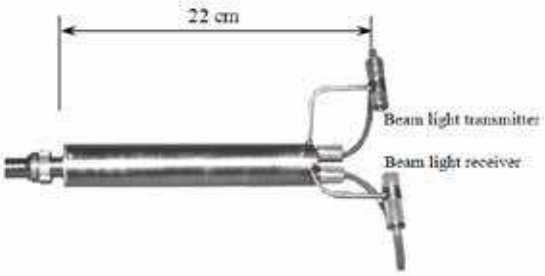

Figure 1: Optical Turbidity Meter (OTM) (KOS'YAN et al., 1995)

An Optical Turbidity Meter (OTM) is designed to carry out experimental turbidimetric measurements in research work (ONISHCHENKO and KOS'YAN, 1989; KOS'YAN et al., 1995; KOS'YAN et al., 2001). This device is based on a reduction of light beam intensity when a light beam passes through water containing suspended sediment according to Buger's law. The electrical and physical parameters of the device are suitably matched according to the recommendations for measuring concentrations in excess of 1 mg/l for particle sizes varying from 50 to 400 μm (for more information, see KOS'YAN et al., 1995). Due to the fact that the light beam emitted from the transmitter of the turbidity meter is weakened by suspended particles rather than being scattered, this method serves as a suitable means of measuring suspended material concentration in the wave-breaking zone or in the inner surf zone, where a vast number of air bubbles are entrained in a mixture of water and suspended sediment and transported together with broken waves towards the shoreline. In this case, the light beam should penetrate the air bubbles. As this is not the case in backscattering methods, the existence of air bubbles is unlikely to affect the measurement of suspended sediment concentrations under such severe conditions. The major limitations of the Optical Turbidity Meter (OTM) are as follows:

- The high sensitivity of OTMs against a murky seawater background due to fine organic, muddy and silty materials tends to increase light beam attenuations.
- Instability of the optical sensors over a long period of use in seawater.
- Selective measurement principle of the optical turbidity meter.
- Difficult calibration procedures.

For more information regarding the technical features of the OTM, see AHMARI (2012).

2.1.4 Previous investigations using the OTM

The Russian-German experiment (Norderney-94), involving the use of the Optical Turbidity Meter (OTM), confirmed the existence of turbulent mechanisms governing sediment suspension and also succeeded in determining the variability scales of the turbulent kinetic energy and the concentration of suspended sediment (KOS'YAN et al., 2001). An analysis of the measured data confirmed the presence of a sharp increase in suspended sediment concentration corresponding to the time of maximum turbulent fluctuations of the cross-shore and long-shore velocities. GRUENE et al. (2007) conducted a series of investigations using the Optical Turbidity Meter (OTM) in the Large Wave Flume (GWK) at the Coastal Research Centre (FZK) in Hanover, which provided an opportunity to reproduce storm dynamic processes in the coastal zone at prototype scale under controlled condi-

tions. The high-frequency fluctuations of suspended sediment particles and the dependency of the suspended sediment concentrations on the form of the wave spectrum are discussed in this investigation. KOS'YAN et al. (2007) used the Optical Turbidity Meter (OTM) to model the vertical distribution of Suspended Sediment Concentration (SSC) above a seabed with small ripples, taking into account the spectral effect of irregular waves with a pronounced group structure. They also checked the reliability of the model using laboratory data from the SISTEX'99 experiment. Generally speaking, the results show a good correlation between the concentrations calculated by the model and the experimental data. The sediment suspension processes in reality, however, are much more complex than the mechanisms considered in this model. In order to improve such models, further experimental and theoretical investigations are required in combination with a consideration of additional processes and an improvement of the measuring devices. For more information, see AHMARI (2012).

2.1.5 Acoustic Backscatter Sensors (ABS)

Acoustic backscatter measurements of sediment concentration using sound scattering methods have been applied more frequently in recent years to measure the instantaneous fluctuations of suspended sediment concentrations under wave action in both field and laboratory investigations and have been validated by many experiments (THORNE et al., 1993, 1995, 2002, 2003a and b, 2007, 2009, ROLAND, 2006; THORNE and CAMPBELL, 1992; VINCENT and GREEN, 1991; GREEN and VINCENT, 1991; THORNTON et al., 1999). Non-intrusive acoustic backscatter measurements can provide a complete profile of the vertical distribution of suspended sediment concentration, thereby offering enhanced temporal and spatial resolution. The backscatter profiler transmits high frequency acoustic energy through the water column. The sample volume is defined by the acoustic beam width and the transmission duration. Suspended particles scatter a part of the acoustic energy back to the transducer. The backscattered signal is measured as a function of range. An inversion algorithm calculates the suspended sediment concentration from the returned backscatter profile. After corrections for water and sediment attenuation, the acoustic backscatter intensity from a uniform field of suspended particles of constant concentration is assumed to be an inverse function of the distance from the source (VAN RIJN, 2006). In order to determine this relationship, it is necessary to calibrate transducers in uniform suspensions. The theoretical background of the acoustics of this device is described in detail by HAY (1983), THORNE and HARDCASTLE (1997) and THORNE and HANES (2002). The ABS typically operates at frequencies between 0.5 and 5 MHz, transmits a short pulse of acoustic energy and provides centimetric resolution for measurements of suspended sediment concentrations in the near-bed region. As the sound pulse is emitted from each transducer, the suspended particles can be insonified. Suspended sediment particles backscatter a part of the acoustic pulse emitted by each probe, while the bed generally reflects a strong echo. The relationship between the received backscatter signals and the characteristics of the suspended material thus provides information on the flow, the suspended sediment particles and the time history of bed forms (VAN RIJN, 1986, 2006). Because the transducer head is located beyond the field of measurement, the acoustic backscatter device yields non-intrusive measurements, and can register suspended sediment fluctuations with sufficient temporal resolution based on the magnitude of the measured backscattered signal. The acoustic backscattering system permits an examination of intrawave and turbulent suspension processes and provides sufficiently accurate measurements of bed location and its temporal variation. VAN RIJN (2006) ex-

plained that at low angles of incidence, the ABS may be used to monitor the formation and evolution of ripples, whereas perpendicular incidence angles provide information on suspended sediment between the sensor head and the seabed level and consequently on the erosion or accretion form of the sediment transport regime above the seabed. The vertical resolution of ABS measurements is limited by the length of the acoustic pulse and the speed at which the signal is digitised and recorded. Van Rijn thus suggested a vertical resolution of about 1 cm. Furthermore, the temporal resolution of ABS measurements depends on the pulse repetition rate and the number of pulses which must be averaged to produce statistically meaningful backscatter profiles. VINCENT and GREEN (1991) used a pulse repetition rate of 10 Hz and averaged the measurements of 4 profiles before storing the data on disc. On average, a profile was recorded every 0.58 s; 1250 average profiles were recorded during each pulse (12 min).

2.1.6 Previous investigations using the ABS

Effect of air bubbles:

VINCENT and GREEN (1991) discussed the difficulty of measuring suspended sediment concentrations using acoustic backscatter instruments in bubbly environments such as near the wave-breaking point and in the swash zone. OSBORNE et al. (1994) performed a number of experiments in the nearshore zone at Stanhope Lane Beach, Prince Edward Island, Canada (water depth of about 1.5 m, sand bed with d_{50} of about 0.23 mm). They were able to show that measurements of suspended sediment concentration outside the breaker zone (with low bubble contamination and organic material content) were relatively consistent. A single-frequency profiling ABS (2.8 MHz) together with an optical backscatter sensor (OBS) was used in these experiments. THORNTON et al. (1999) used an ABS system to determine the vertical profiles of suspended sediment across a barred beach as well as to investigate the vertical coherence length scale, which was found to be an order of magnitude greater than the wave boundary layer. They suggested solving the problem of air bubble effects in terms of the high sensitivity of acoustic backscatter sensors in the water column by analysing the time-averaged concentration profiles, which should show a decreasing concentration with increasing height above the bed. The presence of air bubbles results in an increase of measured concentrations at higher levels, which should be excluded from the analysis. They also suggested an optimum condition for ABS measurements involving uniform fine sand (0.1 to 0.3 mm grain size) under non-breaking wave conditions.

Effect of grain size:

VINCENT and GREEN (1999) performed field measurements on the Continental Shelf (Pacific East Coast of New Zealand) with three transducers (1, 2 and 4 MHz) and a pulse repetition rate of 80 Hz; each profile involved an average of 16 pulses (temporal resolution 5 Hz) and a spatial vertical resolution of 1 cm. They were able to show that the concentration profiles measured by the three transducers are identical, provided the calibration conditions are perfect. This means that the suspended sediment should have the same size distribution at all heights in the water column at the field site and in the laboratory tank. Furthermore, they found that the particle size and suspended sediment concentrations derived from the instrument pair operating at 1 and 2 MHz are the most reliable compared with other combinations. THORNE et al. (2009) illustrated the effect of seabed grain size by

means of acoustic measurements under the same hydrodynamic conditions above fine sand and coarse sand and observed that for fine sand, the seabed behaves dynamically as a plane bed. In the case of coarse sand, however, steep ripples developed on the seabed, causing flow separation at the crests of the ripples followed by leeside vortex generation. They also discussed the way in which sediment entrainment and distribution mechanisms may differ, depending on the seabed structure.

Calibration:

THORNE et al. (2002) used an ABS (including three transducers with frequencies of 1, 2 and 4 MHz) in the large-scale Delta Flume at Delft Hydraulics in the Netherlands to measure near-bed sediment concentration profiles above a rippled sandy bed (d_{50}=0.33 mm) under the action of regular and irregular waves. The results they obtained from the three ABS frequencies were found to be comparable. There were differences, however, due the calibration of the voltage transfer function for the system on the one hand and also due to our present limited knowledge of the variability of the backscattering and attenuation characteristics of the different sediment types. They also used a pump sampler to calibrate the concentrations measured using acoustic transducers and obtained good agreement between the measured concentrations averaged over three ABS-frequencies and the pump sampler concentrations. The differences were found to increase, however, at greater heights above the seabed.

Effect of ripples:

THORNE et al. (2003a) used an ABS in a large flume facility to investigate the sediment entrainment process above vortex ripples beneath regular waves. The observations provided a detailed description of the sediment entrainment process, which is interpreted in relation to the process of vortex formation and shedding. The ABS exhibited consistent temporal and spatial accuracy within the suspension field above the ripples. It was also shown that a standard turbulent diffusion approach, which may be used to predict near-bed time-averaged suspended sediment concentration profiles, will necessarily yield an incorrect description of intrawave physical processes unless modified by the adoption of a non-standard eddy viscosity to represent the eddy shedding process. THORNE et al. (2009) used acoustic backscatter techniques to investigate the form of the sediment diffusivity profile above a rippled bed. The observations were made for slightly asymmetric regular waves above two sandy rippled beds, classified as medium and fine in terms of sand grain size. They showed that in the medium sand case, the steepness of the ripples contributes to flow separation and the generation of vortices on the leeward side of the ripple crest. This is confirmed by the intrawave suspended sediment measurements, leading to a relatively constant mixing length close to the bed. Accordingly, the form of the sediment diffusivity profiles is expected to be constant with height close to the bed ($z \approx k_s$), while above this region ($z > k_s$) the sediment diffusivity is expected to increase linearly with height. A constant region was not detected in the case of fine sand, however; the sediment diffusivity was found to simply increase linearly with height above the bed. VINCENT and GREEN (1991) showed how widely sediment suspension models may differ under different wave and current conditions, and highlighted the fact that seabed roughness has a significant effect on the level of re-suspension.

Range of errors:

GRASMEIJER et al. (2005) carried out a comparative analysis of two acoustic methods (ASTM and ABS operating at three frequencies). The seabed, situated at a local water depth of about h=13 m, consisted of fine sand with d_{50} of about 0.22 mm. The peak tidal velocities were of the order of 0.6 and 0.8 m/s, respectively. These investigations showed that the suspended transport rates derived from the ABS data are somewhat smaller (by a factor of 2) than those determined from ASTM measurements. This result suggests that the ABS tends to underestimate the concentrations of suspended particles smaller than 0.2 mm using transducers operating at a frequency of 2 MHz.

Response to complex wave conditions:

GREEN and VINCENT (1991) analysed the distribution of suspended sediment concentration and the vertical rate of concentration decrease under combined wave action and current flow. GREEN et al. (1995) analysed the wave induced re-suspension of sediment, the influence of wave groups on suspended sediment concentration and the advection of suspension clouds by currents by measuring wave heights, near-bed current velocities, bed shear stresses and suspended sediment concentrations and fluxes during a severe storm using a multi-frequency ABS. THORNE et al. (2007) conducted measurements on a sandy seabed close to the Santa Cruz public pier using acoustic and optical techniques. They compared the measurements of particle size and concentration using a triple frequency acoustic backscatter system (ABS) with those obtained using a commercially available miniature laser scattering and transmissometric instrument (MSCAT). Although they were able to show that the mean grain size estimated by the two methods is the same, they found that the concentration time series showed differences both in magnitude and form. In contrast to the results given by the MSCAT instrument, the ABS data appear to be consistent with wave group observations. They also found that even though the MSCAT measurements are of the same order of magnitude as the ABS measurements, they are in fact greater by a factor of 3.4 and not as clearly related to wave conditions.

2.2 Modelling of suspended load above plane and rippled seabeds

In the nearshore zone, where asymmetric waves predominate and the seabed form changes continuously as a function of the near-bed wave-induced flow regime, the prediction of sediment transport has become an important topic of research, especially in recent years. The predictive capabilities of the developed models are limited, however, and large discrepancies exist between the results of the different models in many cases. A review of the existing prediction models for suspended sediment transport under waves is thus required. This Section hence focuses on analytical and numerical models aimed at describing sediment entrainment processes above both rippled and plane seabeds under similar conditions as those simulated in large wave flume experiments. Under the action of non-breaking waves, where no significant turbulence is generated in the potential flow outside the boundary layer, the sediment particle entrainment process is restricted to:

- the thin near-bed wave boundary layer if the bed is flat or covered with very low ripples, and to
- a layer with a thickness of about 1–2 ripple heights above the ripple crest if the bed consists of steep vortex ripples.

According to NIELSEN (1992), sediment particles in suspension tend to settle out due to the gravity, unless an upward sediment flux (velocity multiplied by concentration) is generated to counterbalance the sediment settling rate. The upward sediment distribution is a consequence of either an organised convective process or a disorganised diffusive process or a combination of both. In the horizontally-averaged approach, the time-dependent sediment distribution comprises a downward component due to gravitational settling ($-w_s\, c$) and an upward component, which consists of a convective or diffusive distribution or a combination of both ($q_D + q_C$). This can be described by the mass conservation equation in the vertical direction as follows (NIELSEN, 1992):

$$\frac{\partial c}{\partial t} = w_s \frac{\partial c}{\partial z} - \frac{\partial q_D}{\partial z} - \frac{\partial q_C}{\partial z} \tag{1}$$

where w_s is the settling velocity, and q_D and q_C are the convective and diffusive sediment fluxes in the vertical direction, respectively, which can be defined as follows:

$$q_D(z,t) = \varepsilon_{s,z} \frac{\partial c}{\partial z} \tag{2}$$

$$q_C(z,t) = p\left(t - \frac{z}{w_c}\right) F(z) \tag{3}$$

where $\varepsilon_{s,z}$ is the turbulent sediment diffusivity coefficient in the vertical direction in a pure diffusive process, which is closely related to the eddy viscosity, ν_t, of the flow. The pick-up tion, $p(t)$, in a pure convective process describes the instantaneous pick-up rate at the seabed while w_c is the average upward convection velocity of a sand particle, which can be assumed to be similar to the convection turbulence velocity, $w_t = \omega\, \delta_{.05}/2.27$, where $\delta_{.05}$ is the boundary layer thickness (NIELSEN, 1992). $F(z)$ is a probability function, which expresses the probability of the entrainment of a sand particle to a level, z_e.The probability function proposed by NIELSEN (1992) is written as follows:

$$F(z) = (1 + z/l)^{-\xi} \tag{4}$$

where l is an appropriate vertical length scale. NIELSEN (1992) suggested a value of 2 for the exponent ξ. For a purely convective process $F(0)$ =1 and for $z \to \infty$, $F(z) \to 0$. NIELSEN (1992) also suggested that sediment entrainment into the water column and the distribution mechanism of suspended sediment concentration can either be described by:

- the diffusive solution if the bed is flat or covered by shorter-crested 2-D/3-D low ripples or mega-ripples, or
- the convective solution if the bed is covered by long-crested 2-D vortex ripples.

Time-dependent sediment entrainment is generally described numerically by means of the Reynolds Averaged Navier-Stokes Equations (RANSE) and the advection-diffusion equation with the following properties:

- It is generally assumed that the velocity of sediment particles in the x-direction is equal to the fluid velocity in the same direction. The only difference between the sediment and fluid velocity in the z-direction is due to the sediment settling velocity w_s ;
- The molecular viscosity is much smaller than the turbulent eddy viscosity $(\nu_m \ll \nu_t)$ which also applies to the sediment diffusivity coefficient: $\varepsilon_m \ll \varepsilon_t$.

There are two types of boundary conditions:

- The reference concentration, c_b, at the reference level, z_b, which reacts instantaneously to changes in the flow velocity near the seabed (usually related to the Shields parameter), $c_b = f(\theta)$, and
- the pick-up function, by which the upward sediment flux or pick-up rate rather than the concentration reacts instantaneously to changes in the flow velocity.

The reference level, z_b, is often assumed to be at the lower limit of the suspended load layer, which is approximately twice the mean sediment grain size ($z_b = 2d_{50}$), and that the bed load transport takes place between the zero-velocity level $z = z_0$ and $z = 2d_{50}$. Despite the large number of data sets available on time-averaged concentrations and ripple dimensions, the number of time-dependent and net transport measurements in large-scale experimental facilities is limited. This means that existing transport models, especially research models, are not sufficiently validated by reliable experimental data. Furthermore, a comparison between operational and research models for sediment transport shows that the largest discrepancies occur in the case of a rippled bed regime. This is due to the complexity of the processes above vortex ripples associated with the phase lags between sediment concentration and orbital velocity as well as the different implementations of near-bed wave-induced flow and the reference concentration (c_b) (DAVIES et al., 2002). Overviews of the transport models for suspended sediment distribution above plane seabeds and rippled seabeds are given in Tables 1 and 2, respectively.

Table 1: Transport models for suspended sediment distribution above a plane bed.

	Model		Parameter	Reference
1	$c(z) = c_0 e^{-z/l}$ $C_0 = \rho_s \gamma \theta_r^3$ $\begin{cases} l = 1.4\eta_r & \text{for} \quad \frac{A_w \omega}{w_s} > 18 \\ l = 0.075 \frac{A_w \omega \eta_r}{w_s} & \text{for} \quad \frac{A_w \omega}{w_s} < 18 \end{cases}$	$\gamma = 0.005$ For flat beds: $\theta_r = \theta' = \frac{\hat{\tau}^2}{((\rho_s - \rho)/\rho).g.d_{50}}$ For rippled beds: $\theta_r = \frac{\theta'}{(1 - \pi \eta_r/\lambda_r)^2}$	l = concentration decay length η_r = ripple height λ_r = ripple length A_w = Amplitude of the near bed orbital excursion ω = wave frequency w_s = still water settling velocity θ' = Effective Shields-parameter	- NIELSEN (1986)
2	if $\varepsilon_s(z) = \kappa u_* z$: $c(z) = c_b \left(\frac{z}{z_b}\right)^{-b}$ if $\varepsilon_s(z) = \kappa u_* z(1 - z/h)$: $c(z) = c_b \left(\frac{z}{z_a} \cdot \frac{h - z_a}{h - z}\right)^{-b}$	$z_b = 2.5 d_{50}$ $b = w_s/\kappa u_*$ (Rouse number) For $d_{50} = 0.13$ mm $b = 1.7$ For $d_{50} = 0.21$ mm $b = 2.1$	ε_s = sediment diffusivity z_b = near bed reference level z_a = κ = Von Karman constant (=0.4) u_* = friction velocity	- BOSMAN and STEETZEL (1988) - VAN RIJN (1993)
3	$c_b(t) = \frac{0.331(\theta - \theta_{cr})^{1.75}}{1 + \frac{0.331}{0.46}(\theta - \theta_{cr})^{1.75}}$ at $z_b = 2.5 d_{50}$		z_b = near bed reference level θ = Shields-parameter θ_{cr} = critical Shields-parameter	- ZYSERMAN and FREDSØE (1994)
4	$c_b = \frac{2.58}{\rho_s} \left(\theta \frac{u_*}{w_s}\right)^{1.45}$ at $z_b = 0.01$ m	$h = 13$ and 20 m	u_* = friction velocity ρ_s = sediment density θ = Shields-parameter	- LEE et al. (2004)

5	$C_b = \frac{0.65}{(1+1/\sigma)^3} \quad at \quad z = 2d_{50}$ $\sigma = \left(\frac{\lvert\theta\rvert - \theta_{cr} - \frac{\pi p_*}{6}}{0.027\lvert\theta\rvert\, s}\right)^{0.5} \quad for\ \lvert\theta\rvert > \theta_{cr} + \frac{\pi p_*}{6}$ $\sigma = 0 \quad for\ \lvert\theta\rvert > \theta_{cr} + \frac{\pi p_*}{6}$	$\nu_t = \varepsilon_s$ $p_* = \left[1 + \left(\frac{\pi/6}{\lvert\theta\rvert - \theta_{cr}}\right)^4\right]^{-1/4}$ $s = \rho_s/\rho$ $\theta_{cr} = 0.045$	d_{50} = median grain size θ = Shields-parameter θ_{cr} = critical Shields-parameter ε_s = sediment diffusivity ν_t = turbulent eddy viscosity	- DAVIES and LI (1997) - Fredsoe et al. (1985)
6	$c(0,t) = A_0 p(t)$ $p(t) = 3.3\left(\frac{\theta'(t) - \theta_{cr}}{\theta_{cr}}\right)^{1.3} \frac{\left(\frac{\rho_s}{\rho} - 1\right)^{0.6} g^{0.6} d^{0.8}}{\nu^{0.2}}$	$A_0 = 0$ or 1	ρ_s = sand density ρ = water density ν = kinematic viscosity θ' = Shields-parameter θ_{cr} = critical Shields-parameter d = sediment grain diameter g = acceleration due to gravity	-KOS'YAN et al. (2007)
7	$c(z) = C_0\, exp(-\alpha z)$ $\alpha = \frac{1}{h} exp(0.396)\left(\frac{H}{H_0}\right)^{2.740}\left(\frac{h}{H_0}\right)^{-2}\left(\frac{H_0}{w_s T}\right)^{0.211}$ $C_0 = \rho\, exp(-4.159)\left(\frac{h}{H_0}\right)^{-1}\left(\frac{H}{H_0}\right)^{1.863}\left(\frac{H_0}{w_s T}\right)^{-0.137}$	correlation coefficient for α: $r = 0.929$ correlation coefficient for C_0: $r = 0.762$	H = local wave height H_0 = wave height in deep water h = water depth w_s = sediment fall velocity ρ = water density r = correlation coefficient	-PETERS et al. (2000)

Table 2: Transport models for suspended sediment distribution above a bed with steep vortex ripples.

	Model		Parameter	Reference
1	Turbulent closure model	- reference concentration, C_0, of Fredsoe et al. (1985) - $\varepsilon_s = \nu_t$	ε_s = sediment diffusivity ν_t = turbulent eddy viscosity	- DAVIES and THORNE (2002)
2	1DV transport model under waves	- reference concentration, C_0, of Fredsoe et al. (1985) - $\nu_t = \kappa^2 z^2 \left\|\frac{\partial u}{\partial z}\right\|$ - $k_s = 25\,\eta^2/\lambda_r$ - $\nu_t = \beta\,\varepsilon_s$	κ = Von Karman constant (=0.4) η_r = ripple height λ_r = ripple length ν_t = turbulent eddy viscosity ε_s = sediment diffusivity β =user defined parameter	- RIBBERINK and AL- SALEM (1995)
3	2DV sediment transport model	- reference concentration, C_0, of Fredsoe et al. (1985) - $\varepsilon_s = \nu_t$	ε_s = sediment diffusivity ν_t = turbulent eddy viscosity	- ANDERSEN (1999)
4	2VD suspended sediment and flow model	- $\varepsilon_s = 3/4\,\nu_t$	ε_s = sediment diffusivity ν_t = turbulent eddy viscosity	- HUYN THANH et al. (1994)
5	$w_s c + \varepsilon_s \frac{\partial c}{\partial z} - w_s c_0 F(z) = 0$ $F(z) = (1 + z/l)^{-\xi}$ $\Phi(z) = e^{-w_s z/\varepsilon_s}\left[1 + \frac{w_s}{\varepsilon_s}\int_0^z e^{-w_s z'/\varepsilon_s}(1 + z'/l)^{-2} dz'\right]$	- when purely diffusive mechanism: $\Phi_d(z) = e^{-w_s z/\varepsilon_s}$ - when purely convective mechanism: $\Phi_c(z) = (1 + z/l)^{-2}$	$\xi = 2$ w_s = sediment fall velocity l = concentration decay length ε_s = sediment diffusivity	- THORNE and WILLIAMS (2002)

6	1DV transport model under waves: (a) In the lower level $z < 2\eta_r$ $\frac{\partial\langle c\rangle}{\partial t} = \frac{\partial}{\partial z}\left(w_s\langle c\rangle + K_s\frac{\partial\langle c\rangle}{\partial z}\right)$	- For weakly asymmetrical waves the eddy viscosity: $K_s = \overline{K}\left((1+\varepsilon_0) + \varepsilon_1 e^{i\omega t} + \varepsilon_2 e^{i\omega t}\right)$ $\overline{K} = c_K A\omega\, k_s$ c_K =0.004	K_s= Sediment diffusivity w_s = sediment fall velocity $\varepsilon_1 = \lvert\varepsilon_1\rvert e^{i\varphi_1}$ $\varepsilon_2 = \lvert\varepsilon_2\rvert e^{i\varphi_1}$ k_s = equivalet bed roughness orbital excursion	- DAVIES and THORNE (2005)
	(b) In the upper layer ($z > 2\eta_r$) $\frac{\partial\langle c\rangle}{\partial t} = \frac{\partial}{\partial z}\left(w_s\langle c\rangle + \varepsilon_s\frac{\partial\langle c\rangle}{\partial z}\right)$	-$\varepsilon_s = \beta\nu_t$ where: $\beta = 4.0 - 3.0\left(\frac{z-2\eta_r}{h-2\eta_r}\right)^{\zeta}$	ε_s = sediment diffusivity ν_t = turbulent eddy viscosity w_s = sediment fall velocity η_r = ripple height h =water depth ζ =0.4	
7	Asymmetrical waves: $c_b = G\left(\frac{\hat{u}_c^{3.5}}{4TT_c} + \frac{\hat{u}_t^{3.5}}{4TT_t}\right)$ Irregular waves: $c_b = G\frac{\hat{u}_{eff}^{3.5}}{T_p^2}$	$G = 3000 \pm 8\ kgm^{6.5}s^{5.5}\hat{u}_{eff} = 1.62\sqrt{m_0}$	$\hat{u}_c$ = maximum velocity under wave crest $\hat{u}_t$ = maximum velocity under wave trough T_c = crest period T_t = trough period T_p = peak period of the wave spectrum m_0 =variance of the velocity signal	RIBBERINK (1987)
8	$c_n(z,t) = \sum_0^N \zeta_n c_n\, e^{in\omega t}$	$\zeta_n = e^{-\frac{w_s}{\varepsilon_s}\alpha_n}$ $\alpha_n = \frac{1}{2} + \sqrt{\frac{1}{4} + i\frac{n\omega\varepsilon_s}{{w_s}^2}}$	$c_n = \frac{P_n}{w_s a_n}\, e^{-in\psi_n}$ w_s = sediment fall velocity ε_s = sediment diffusivity P_n= The n-th harmonic of pick-up function ($p(t)$)	NIELSEN (1979)

3. Large-scale experiments in the Large Wave Flume (GWK)

Nearshore sediment transport in relation to different wave and seabed regimes is of a complex nature. In order to gain a better understanding of this complexity, a number of experimental studies have been performed in the past (mainly in the field). Due to the enormous difficulties associated with field measurements (e.g. non-controllable transducer positions from a mobile seabed, uncertainties in ripple measurements, and interactions between the measured flow and the seabed, etc.), controlled large-scale experiments at near-prototype scale have proved to be more efficient for studying and understanding suspended sediment processes. For this reason, a series of new prototype-scale experiments have been carried out in the Large Wave Flume (GWK) which focus on time-dependent sediment transport processes above rippled and plane seabeds under the action of non-breaking and near-breaking regular and irregular waves. The acoustic backscattering technique, ABS, was deployed to determine seabed profile evolution and to measure and analyse small-scale sediment entrainment processes.

3.1 Overall approach and measurement phases

In general, the experiments carried out in the Large Wave Flume (GWK) can be divided into two distinct phases as follows:

- Phase 1: Comparative analysis of measuring techniques (Test group 1 in Figure 2).
- Phase 2: Intrawave suspended sediment concentration analysis using the most appropriate measuring devices proven in Phase 1 (Test groups 2, 3 and 4 in Figure 2).

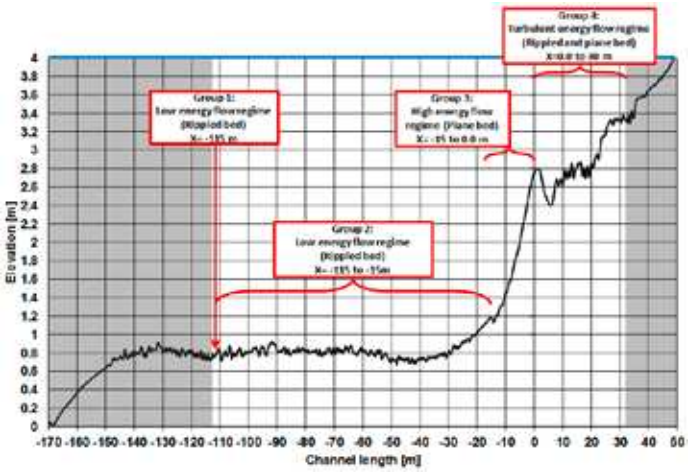

Figure 2: Longitudinal beach profile in Large Wave Flume (GWK) in an equilibrium condition showing four test groups in terms of the prevailing hydro- and morphodynamic conditions

The four groups of experiments depicted in Table 3 can be classified as follows:

Group 1 of experiments

included 33 test series with 13200 waves in three different wave height categories (H,H_s=0.8, 1.0 and 1.2 m, T, T_p=5s, γ=1.0-9.9) at a fixed measuring point using a fixed test frame (distance from the wave paddle 111.45 m and from the bar position -115 m; see Figure 2) to carry out an extensive comparative analysis using different measurement techniques and to study the effect of peak enhancement factor, γ, in case of tests using JONSWAP-spectra, on the suspended sediment entrainment. The test conditions for the experiments in group 1 is summarised in Table 3 and the measuring station is depicted in Figure 2.

Group 2 of experiments

included 3 tests in each measuring station with regular waves (H=1.0m, T=5s) and JONSWAP spectra (H_s= 0.8, 1.0m; T_p=5 and 7s; γ=3.3) every 20 m towards bar area using a movable instrumentation frame from point X= -115 m to X=-15 m in non-breaking wave zone (see Figure 2). The test conditions for the experiments in group 2 are summarised in Table 4 and the measuring station is depicted in Figure 2.

Group 3 of experiments

included 3 tests in each measuring station with regular waves (H=1.0m, T=5s) and JONSWAP spectra (H_s= 0.8, 1.0 m; T_p=7 and 5s; γ=3.3) using the movable instrumentation frame from point X= -15 m to X=±0.0 m (bar position) above plane bed beneath strong asymmetric near-breaking waves. The test conditions for the experiments in group 3 are summarised in Table 4 and the measuring station is depicted in Figure 2.

Group 4 of experiments

included three tests in each measuring station with regular waves (H=1.0m, T=5s) and JONSWAP spectra (H_s= 0.8, 1.0 m; T_p=7 and 5s; γ=3.3) using the movable instrumentation frame from X=±0.0 m (bar position) to X=30 m above rippled and plane bed beneath breaking and broken waves. The test conditions for the experiments in group 2 are summarised in Table 4 and the measuring station is depicted in Figure 2.

Table 3: Summary of test conditions for the three test series of group 1 shown in Figure 2.

Test group	Wave type	H, H_s [m]	T_p [s]	Water depth h [m]	Flow regime		Bed form	Distance from wave paddle [m]	Distance from bar X [m]
					Near bed zone	Boundary layer			
1-1	Regular waves, JONSWAP (γ=1.0-9.9)	0.8	5	3.20	Low energy	Turbulent rough	Rippled bed (2D-3D ripples)	111.45	-115
1-2	Regular waves, JONSWAP (γ=1.0-9.9)	1.0	5	3.20		Turbulent rough	Rippled bed (2D-3D ripples)	111.45	-115
1-3	Regular waves, JONSWAP (γ=1.0-9.9)	1.2	5	3.20		Turbulent rough	Rippled bed (2D-3D ripples)	111.45	-115

Table 4: Summary of test conditions for the three test series of groups 2.4 shown in Figure 2.

Test group	Wave type	H, H_s [m]	T_p [s]	Water depth h [m]	Flow regime		Bed form	Distance from wave paddle [m]	Distance from bar X [m]
					Near bed zone	Boundary layer			
2	Regular waves	1.0	5	3.20	Low energy	Turbulent rough	Rippled bed (2D-3D ripples)	111.45 to 205	-115 to -15
	JONSWAP (γ=3.3)	0.8	7	3.20			Rippled bed (2D-3D ripples)	111.45 to 205	-115 to -15
	JONSWAP (γ=3.3)	1.0	5	3.20			Rippled bed (2D-3D ripples)	111.45 to 205	-115 to -15
3	Regular waves	1.0	5	1.20 to 2.80	High energy	Turbulent rough	Plane bed	205 to 220	-15 to 0.0
	JONSWAP (γ=3.3)	0.8	7	1.20 to 2.80			Plane bed	205 to 220	-15 to 0.0
	JONSWAP (γ=3.3)	1.0	5	1.20 to 2.80			Plane bed	205 to 220	-15 to 0.0

4	Regular waves	1.0	5	0.60 to 1.60	High turbulent	Turbulent rough	Rippled bed (2D-3D ripples)	220 to 250	0.0 to 30
	JONSWAP (γ=3.3)	0.8	7	0.60 to 1.60			Rippled bed (2D-3D ripples)	220 to 250	0.0 to 30
	JONSWAP (γ=3.3)	1.0	5	0.60 to 1.60			Rippled bed (2D-3D ripples)	220 to 250	0.0 to 30

3.2 Model setup

In both experimental phases the concrete bottom of the GWK flume was covered with a sand layer representing the seabed. Four tests with different wave parameters, comprising well-sorted sand (GWK sand) with $d_{50} = 0.242$ mm and a non-uniformity factor of $U = d_{60}/d_{10} = 2.24$, were performed in 2008.

3.3 Instrumentation

The following devices were used in the GWK experiments:

- Transverse Suction System (TSS) with 5 intake nozzles mounted at the points shown in Figure 3 a above the seabed for time-averaged measurements of suspended sediment concentrations
- Multifrequency Acoustic Backscatter Sensors (ABS, type: Aquascatt) (2 instruments) for measuring the temporal-spatial vertical distribution of suspended sediment concentration and the bed location time series (Figure 3 c).
- Optical Turbidity Meter (OTM) (4 instruments) for measuring suspended sediment concentrations at given heights above the seabed (Figure 3 d).
- Electromagnetic Current Meter (ECM) manufactured by "Norddeutsche Seekabel Werke (NSW)" (5 instruments) for simultaneous measurements of the vertical and horizontal components of the wave-induced orbital flow velocities at the given heights above the seabed (Figure 3 b).
- Wave gauges (22 instruments) for simultaneous measurements of the free water surface elevation along the entire beach profile including the measurement points.

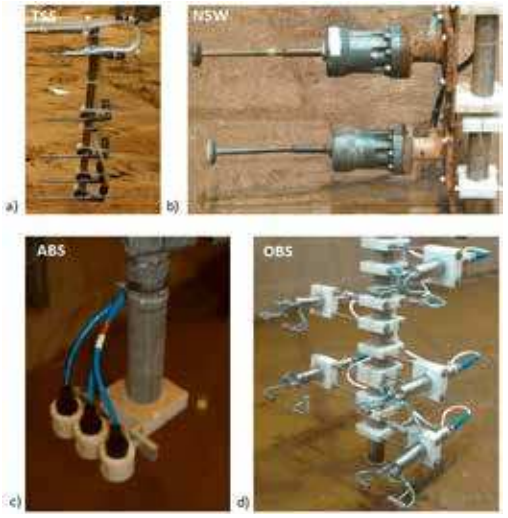

Figure 3: Sensors used in the GWK experiments: a) Intake nozzles of the Transverse Suction System (TSS); b) Velocity sensors (Electromagnetic Current Meters, ECMs); c) Acoustic Backscatter Sensors (ABS) and d) Optical Turbidity Meters (OTMs)

Table 5 summarises all of the instrumentation deployed in the tests for measuring suspended sediment concentrations and instantaneous hydrodynamic parameters and their sampling rates. For more details, see AHMARI (2012).

Table 5: Instrumentation and sampling rates.

Measurement characteristics	Instrumentation	Remarks	Sampling rate
Free water surface elevation (η)	Wave Gauges (WGs)	-18 gauges along the flume -1 gauge at each measurement point	40 Hz
Wave-induced orbital velocity (u, w)	Electromagnetic Current Meter (ECMs)	-3 sensors at the wall of the flume -2 sensors at the measurement point near the bed	40 Hz
Suspended Sand Concentration (SSC)	Transverse Suction System (TSS)	-5 nozzles at different levels above the sand bottom	-Extraction of water and sediment: 20 min. -Nozzle speed: 1.5 m/s
	Acoustical Backscatter System (ABS)	-3 transducers with different frequencies (1.0, 2.0, 4.0 MHz) Operation range: 80 cm above the sand bed	-Number of bins: 100 -Spatial resolution: 0.01 m -Sampling rate: 4 Hz
	Optical Turbidity Meter (OTMs)	-4 transducers mounted at differen levels above the sand bed at two beams	40 Hz

3.4 Testing programme and procedure: Phase 1

Phase 1 of the experiments included measurements of the temporal-spatial distribution of suspended sediment concentrations (SSC) above a moveable sand bed using mechanical, optical and acoustic techniques for comparative purposes. Also included were simultaneous measurements of water surface elevations and the vertical and horizontal components of orbital flow velocity induced by non-breaking regular and irregular waves above a rippled seabed over the horizontal part of the beach profile. For this purpose, a fixed instrumentation frame was installed at a measuring station located at 114.45 m in front of wave paddle (see Figure 4). The first aim of the experiments was to carry out a comparative analysis of the different measuring techniques in order to identify the most appropriate measuring device regarding sufficient spatial and temporal accuracy. The second aim of this experimental phase was to measure and analyse the effects of the peak enhancement factor on the suspended sediment concentration entrainment process for the case of irregular waves (JONSWAP spectra).

Hydrodynamics:

The experiments were performed under the action of regular and irregular waves (JONSWAP spectra). The peak period was kept constant (T or T_p=5s) whereas the peak enhancement factor γ was varied from γ=1 to 9.9 to investigate the influence of the increasing power spectral density of different JONSWAP spectra compared to the completely developed reference spectrum (P.M.) represented by the coefficient γ, which has not yet been fully account for in previous studies. Moreover, the instantaneous free water surface elevations as well as the wave-induced orbital velocity components were measured simultaneously with suspended sediment concentrations during each test. Measurements were performed in each test for almost 400 waves with a total duration of about 35 min. The water depth above the concrete bottom of the wave flume was 4 m, corresponding to a still water depth above the sand bed in the range of 3.15 to 3.22 m depending on the instantaneous seabed profile evolution at the measuring station. The peak wave period T_p=5 s was held constant in each test. The two components of the intrawave orbital flow velocity (u and w) were measured using two Electromagnetic Current Meters (ECMs) at two different levels above the seabed. In order to avoid any disturbance of the mobile seabed during intrawave hydrodynamic forcing in the near-bed zone, the first ECM was mounted at 0.25 m above the initial seabed level. This elevation is low enough to record the intrawave velocity above the expanded wave boundary layer over a rippled seabed. The second ECM was then mounted at 0.2 m above the first one (0.45 m above the seabed) to record the velocity time series at a higher elevation in the ambient flow.

The free water surface elevation, η, was measured simultaneously by means of a Wave Gauge (WG) located at a measuring station 111.45 m in front of the wave paddle (see Figure 4).

Morphodynamics:

Prediction models for sediment transport above seabeds covered with ripples, dunes and sand waves require the geometry of sedimentary structures as input, which is mostly expressed by their steepness (e.g. ripple steepness, η_r/λ_r, where η_r is the ripple height and λ_r, the ripple length). According to GRANT and MADSEN (1982), steep ripples ($\eta_r/\lambda_r > 0.1$) are responsible for the major

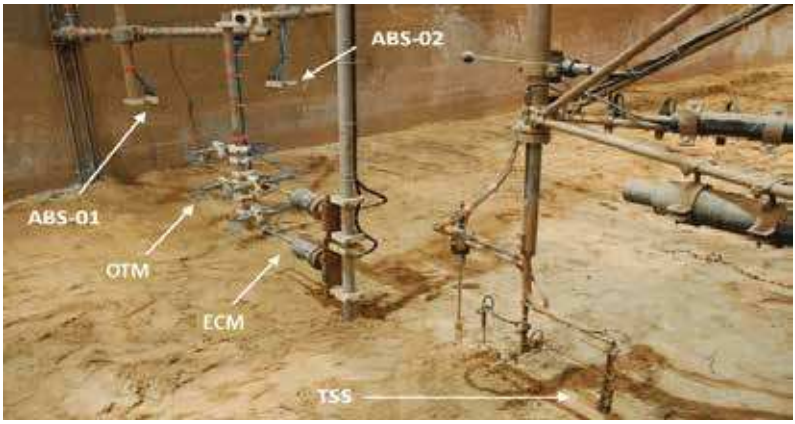

Figure 4: Location of the measuring devices used in the Phase 1 experiments

part of bed roughness under oscillatory flow conditions. Depending on the model and the required accuracy, ripple geometry may have an influence on the calculation of bed roughness, the prediction of seabed formations, the near-bed flow regime or the detailed behaviour of sediment entrainment and transport above sedimentary structures. In general, the sedimentary structures induced by non-breaking regular and irregular waves, as observed in the presented large-scale GWK experiments, can be divided in two main groups:

[1] Long ripples under quasi-equilibrium conditions η_r/λ_r <0.08):

As confirmed by many field and laboratory experiments, ripple geometry requires sufficient time to become established (equilibrium ripples) and change the near-bed flow condition at any instant (DOUCETTE and O'DONOGHUE, 2002; O'DONOGHUE and CLUBB, 2001). Quasi-equilibrium sand ripples are long seabed structures formed below previously more energetic waves and do not adjust themselves to prevailing flow conditions (HANES et al., 2001). Depending on the mobility number, an equilibrium condition requires many hours to become established. In the presented large-scale experiments it was found that a quasi-equilibrium condition is approximately attained after a time period of about 15 hours (Test group 1 with mobility ψ<100 (see Section 5), H, H_s= 0.8, 1.0, 1.2 m, T,T_p=5s).

The GWK mechanical beach profiler is a mechanical profiler with a length of 7.60 m. The depth of penetration into the sand caused by the dead weight of the sensor arm was found to be in the range of 2 to 20mm. Owing to this loss of bed profile, which is crucial with regard to ripple development under laboratory conditions in the wave flume (η_r =0-15 cm and λ_r =0-100 cm), this method of bed profiling is not accurate enough to investigate ripple geometry under non-equilibrium conditions when considering the effect of ripple steepness, which is an important factor in any study of sediment transport above rippled seabeds. Assuming a mean seabed profile loss of about 10 mm, measurements of bed profile evolution at the measuring station using the mechanical seabed profiler revealed the permanent appearance of rounded regular long ripples (3-D low ripples, 0.08≤ η_r/λ_r ≤ 0.12; where η_r and λ_r are the ripple height and ripple length, respectively) partly superimposed on irregular 2-D steep ripples (η_r/λ_r >0.12).

Empirical formulae based on field and laboratory experiments have been developed which take into account the effects of flow and sediment parameters on ripple geometry (ripple steepness)

(NIELSEN, 1981, 1992; GRANT and MADSEN, 1982; VAN RIJN, 1989; WIBERG and HARRIS, 1994). Such formulae only seem to be valid, however, over the specific range of conditions upon which they are based. A large number of such formulae are based on empirical data from wave flume experiments involving short periodic waves with low amplitudes. Ripples, which are not fully developed under such conditions, are found to reach equilibrium with hydrodynamic forcing. These models have not been applied so far to large-scale laboratory experiments with prototype periods and orbital amplitudes (VAN DER WERF, 2006; O'DONOGHUE and CLUBB, 2001). An attempt has been made, however, to demonstrate the approximate development of ripple geometry under quasi-equilibrium conditions induced by irregular and regular non-breaking waves along a rippled sand profile using the predictive formulae of NIELSEN (1992). For more details, see AHMARI (2012).

[2] Ripples under non-equilibrium conditions ($0.10 < \eta_r/\lambda_r$):

Non-equilibrium ripples are 2-D and 3-D steep and low sedimentary structures which have not yet reached the equilibrium condition and migrate predominantly in the onshore direction under the action of regular non-breaking asymmetrical waves (DOUCETTE and O'DONOGHUE, 2002). As mentioned above, the time-averaged beach profile measured with the GWK mechanical bed profiler was not sufficiently accurate to register the steepness of the migrated non-equilibrium ripples, which is essential regarding sediment entrainment processes and the near-bed flow regime. Figure 5 shows the steep ripples in a non-equilibrium condition observed after completion of the tests. The empirical formulae are unable to predict ripple steepness correctly, as an average error of 37 to 55 percent was found in the prediction of ripple steepness under non-equilibrium conditions (JETTE and HANES, 1996). This could be due to errors in the previously collected data sets used to construct these models, or to gaps in our present knowledge of the mechanics of ripple formation and geometric equilibrium within the flow field (DOUCETTE and O'DONOGHUE, 2002).

Figure 5: Ripples observed immediately after the tests in a non-equilibrium condition with onshore migration

An important advantage of the ABS measuring technique is the ability to detect the bed location in conjunction with measurements of the concentration event. This is unique, especially regarding the determination of the reference concentration, C_0. Moreover, the bed location is the clue for detecting the differences between measured and predicted profiles of suspended sediment concentration. Changes in bed location are revealed by an increase in signal amplitude and any variation in the form of the ABS measurement time series when the bed response contaminates a range bin (THORNE et al. 2002). By means of a quantitative analysis of the behaviour of steep non-equilibrium ripples, which migrate onshore beneath the ABS, it was possible to track the ripple height (η_r) from clearly-defined

echoes of the ABS return signals at the three ABS frequencies over the measurement time series for each test run.

Mobile sediment:

Suspended sediment concentration was measured using the 1.0, 2.0 and 4.0 MHz ABS transducers over a time period of about 35 min for each test series at an operating height of about 0.8 m above the seabed with a spatial resolution of 0.01 m. An explicit acoustic inversion (THORNE and HANES, 2002) was carried out on the averaged recorded backscatter voltages to convert the measured acoustic signals into concentration values. Optical Turbidity Meters (OTMs) were also used to simultaneously measure temporal and spatial suspended sediment concentration fluctuations at given points above the seabed. Time-averaged pump-sampled concentrations measured by the TSS were also used to conduct a comparative analysis between the mechanical time-averaged concentrations and the calculated time-averaged and bed-averaged concentrations based on the ABS and OTM data sets.

3.5 Testing programme and procedure: Phase 2

The sediment transport problem can in fact be imagined as a triad of three interacting components (THORNE et al., 2002): seabed morphology (e.g. bed forms), hydrodynamic forcing (e.g. currents, waves) and mobile sediment (e.g. suspended sediment). Each solution of the sediment transport problem requires the determination of these triad-components and a precise knowledge of the interaction between them. Due to the restrictions of previous experiments concerned with the measurement of suspended sediment concentration, which have mostly been performed under limited hydrodynamic and geomorphological conditions, a new series of large-scale experiments were carried out in the present study. The aim of these experiments was to extensively measure sand transport processes both temporarily and spatially under non-breaking and near-breaking regular and irregular wave action covering a wide range of near-seabed hydrodynamic-morphological interactions in the nearshore zone. The procedure adopted in the new experiments, which focus on the measurement of time-dependent suspended sediment concentration along the entire beach profile reproduced in Large Wave Flume (GWK), is described in the following:

In order to achieve the goal of the Phase 2 experiments, acoustic concentration measurements were performed using the ABS device as the most suitable measuring device identified in Phase 1. The major purpose of these measurements was to identify and record small-scale entrainment processes above a sandy seabed. The experiments also included simultaneous measurements of water surface elevations, η, as well as wave-induced near-bed orbital flow velocities. A TSS instrument was also used to measure the time-averaged concentration at four different heights above the seabed during each test. The measurements were performed along the entire beach profile starting from the first measuring station above the shoaling and breaking zone and extending to the inner and outer surf zones (groups 2, 3 and 4 of the experiments listed in Table 4). A moveable steel-frame with stilts was used to support the measuring devices and also to provide sufficient flexibility for measurements along the entire beach profile (see Figure 6). For more details, see AHMARI (2012).

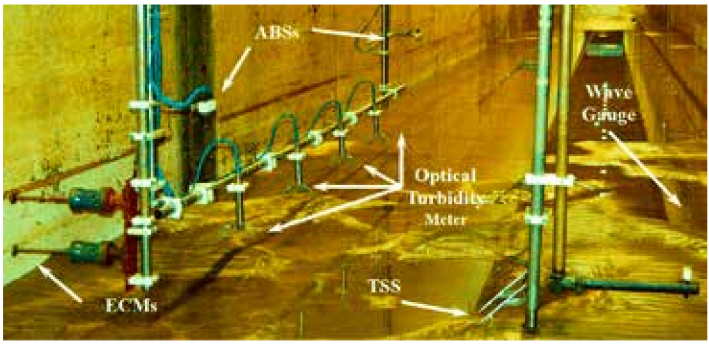

Figure 6: Location of the measuring devices used in Phase 2 of the experiments

4. Comparative analysis of suspended sediment concentration measurements

Several experiments in the past have been performed using mechanical, optical and acoustic devices to measure and analyse suspended sediment transport in the nearshore zone (see Section 2.5). In some of these experiments using mechanical devices, such as the pump sampling system, it was only possible to measure time-averaged concentrations of suspended sediment at selected heights above the seabed. Other more advanced techniques (optical devices, acoustic devices, laser technique) have also been applied to measure the time series of suspended sediment concentration fluctuations at single points above the seabed. New-generation measuring devices (acoustic backscattering systems, optical techniques and laser devices) have been used more recently to study further details of the temporal entrainment of sediment particles due to intrawave processes above sandy seabeds. Process-oriented sediment transport models have also been developed in recent years to represent details of temporal and spatial sediment transport processes under the action of waves and currents. Small-scale sediment entrainment processes and suspended sediment distribution mechanisms, especially above rippled seabeds, and the temporal and spatial interactive effects of both rippled structures and the near-seabed hydrodynamic regime on mobile sediment transport are complex in nature. For this reason, it is necessary to comparatively analyse the different techniques for measuring suspended sediment concentration induced by waves, with the objective of identifying the most appropriate technique capable of consistently monitoring the interactive processes near the seabed with sufficient temporal and acoustic accuracy. A comparative analysis of the results obtained by the Transverse Suction System (TSS), multi-frequency Acoustic Back-scattering Sensors (ABS) and the Optical Turbidity Meter (OTM), as discussed in Section 3, will now be described with the afore-mentioned objectives in the following Sections.

4.1 Experimental results

Simultaneous measurements of suspended sediment concentrations using an acoustic device (ABS), a mechanical device (TSS) and an optical device (OTM) were performed in the Large Wave Flume (GWK). One of the important goals of the experiments in phase 1 was basically to capture the representative concentration data for a comparative analysis between three measuring devices in two

directions. One was focused on the time-averaged sand transport processes over rippled beds under regular and irregular flows covering a wide range of hydrodynamic and morphological conditions. The other was focused on the time-dependent sediment transport processes over rippled seabeds, in particular, on the combined time-dependent velocity and concentration field under regular weakly asymmetric flows. These new experiments are described in the following Sections.

4.2 Time-averaged measurements

The time-averaged vertical distribution of suspended sediment concentration using all three devices is illustrated by way of example in Figures 7 and 8 (ABS measurements: closed white circles; OTM measurements: closed red circles and TSS measurements: closed triangles). As can be seen in Figure 7, the ABS device provides a complete vertical profile of the suspended sediment concentration over a defined vertical operating range up to the transducer head. The ABS transducers operate in a mono-static mode (the transducers operate simultaneously as transmitters and receivers). The acoustic signals were superposed with a pulse repetition rate of 128 Hz for each transducer and the backscattered signals were averaged in terms of hardware over 32 profiles to yield a temporal resolution of 0.25 s (4 Hz). The spatial resolution (bin size) for the test series was 0.01 m and the operating range was 0.8 m above the initial sandy bottom. The concentrations measured by Optical Turbidity Meters (OTMs) (red closed circles in Figure 7) were averaged over duration of about 20 minutes during each test run. The TSS measurements (black triangles) were also performed over a time period of about 20 minutes during each test. Figure 7 a shows the time-averaged vertical concentration profile for a test performed with irregular waves (JONSWAP spectrum, H_s=1.2m, T_p=5s), whereas Figure 7 b shows the time-averaged vertical distribution of suspended sand concentrations induced by non-breaking regular waves (H =1.2m, T =5s). The figures clearly illustrate an exponential decrease in suspended sediment concentration towards the water surface. Moreover, Figure 8 shows the effect of wave height on the vertical distribution of time-averaged and bed-averaged suspended sediment concentrations above the seabed. As is evident in the figures, increasing wave height induces an increase in momentum transfer at higher elevations, which consequently results in higher suspended sediment concentrations. Figures 7 and 8 show that the rapid decrease in suspended sediment concentration takes place in a near-bed region with a thickness of about 20 cm (Layer 1). Above this height (Layer 2), the rate of decrease in suspended sediment concentrations is much lower than in the first layer. Due to the fact that the seabed was rippled under the prevailing hydrodynamic regime, this significant difference between the decreasing slope of the vertical distribution profile corresponds to the influence of steep ripples, which modifies the near-bed intrawave flow regime and consequently affects the sediment entrainment mechanisms above rippled beds.

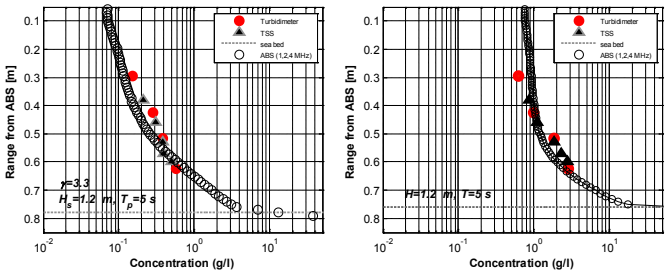

Figure 7: Time-averaged and bed-averaged ABS (closed white circles), Optical Turbidity Meter (closed red circles) and TSS (black triangles) measurements of suspended sediment concentration: a) for a JONSWAP spectrum (H_s=1.2 m, T_p= 5 s, γ=3.3) and b) for regular waves (H=1.2 m, T= 5 s)

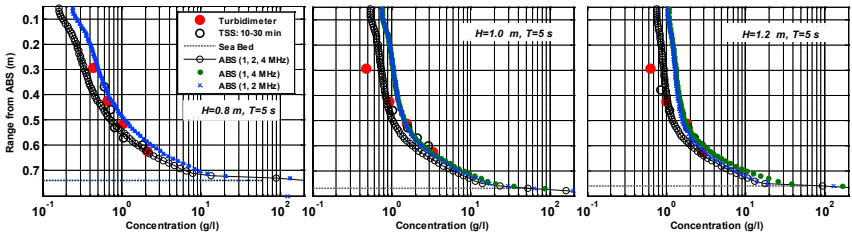

Figure 8: Effect of wave height on the vertical time-averaged and bed-averaged concentration profiles measured by the ABS at different frequencies (1,2,4 MHz; 1,2 MHz and 1,4 MHz), Turbidimeter (red dots) and TSS (white circles) for regular waves with h=3.18 m, H=0.8, 1.0, 1.2 m, T=5

A statistical analysis aimed at quantifying the close agreement between the acoustic and optical measurements is discussed in the following. Figures 9 a, b, c show the regression plots between "acoustic" concentrations (C_{ABS}), "optical" concentrations (C_{OTM}) and "pump-sampled" concentrations (C_{TSS}) carried out at different heights above the sandy bed under the action of regular and irregular waves (H_s, H =0.8, 1.0, 1.2 m; T, T_{p_s}, H =5s). Linear regressions on the data yielded the correlation coefficients R^2 = 0.9444, 0.9679 and 0.9744 for the C_{ABS}-C_{TSS} plot, R^2 = 0.98, 0.99 and 0.9935 for the C_{OTM} -C_{TSS} plot, and R^2 = 0.8884, 0.9117 and 0.9124 for the C_{OTM} - C_{ABS} plot for Hs =0.8, 1.0 and 1.2 m, respectively. As can be seen in Figure 9 a, the mean concentrations lie very close to the C_{ABS} - C_{TSS} regression line. In the case of the ABS measurements, the regression gradients for the 3 wave heights were C_{ABS} /C_{TSS}=0.9884, 0.9944, 0.9337, respectively, which shows that there is no significant scatter from the C_{ABS} - C_{TSS} regression line. Moreover, Figure 9 b shows a comparison between the time-averaged concentrations measured by the OTM and the TSS. As the OTM and TSS intake nozzles were not mounted at the same heights above the seabed, a one to one comparison between them was not possible. The data measured by the first and the third TSS nozzles mounted at 12 cm and 26 cm above the seabed, respectively, could however be reasonably compared with the concentrations measured by the first and the second turbidity meters located at 14 cm and 28 cm above the seabed, respectively. Good agreement is generally observed between the time-averaged C_{TSS} and $C_{OTM,}$ especially at concentrations below 1 g/l. The regression analysis shows, however, that the mean concentrations measured by the turbidity meters generally tend to be overestimated compared with the TSS concentrations, which is more pronounced at higher concentrations (the regres-

sion gradients for the 3 wave heights were C_{OTM} /C_{TSS}=1.12, 1.1157 and 1.0607, respectively). This discrepancy may be partly explained by the larger attenuations at higher concentration levels due to the re-suspension of more muddy and silty materials. Finally, Figure 9 c shows the regression analysis between the time-averaged concentrations measured by the ABS and OTM. The regression gradients (C_{OTM} /C_{ABS}=1.1333, 1.1088 and 0.1164 for the 3 wave heights, respectively) indicate a small overestimation of C_{OTM} compared to C_{ABS}, particularly at higher concentrations. This may be explained by the steady background concentrations measured by the OTMs. The corresponding correlation coefficients were found to be R^2= 0.8884, 0.9117, 0.9124.

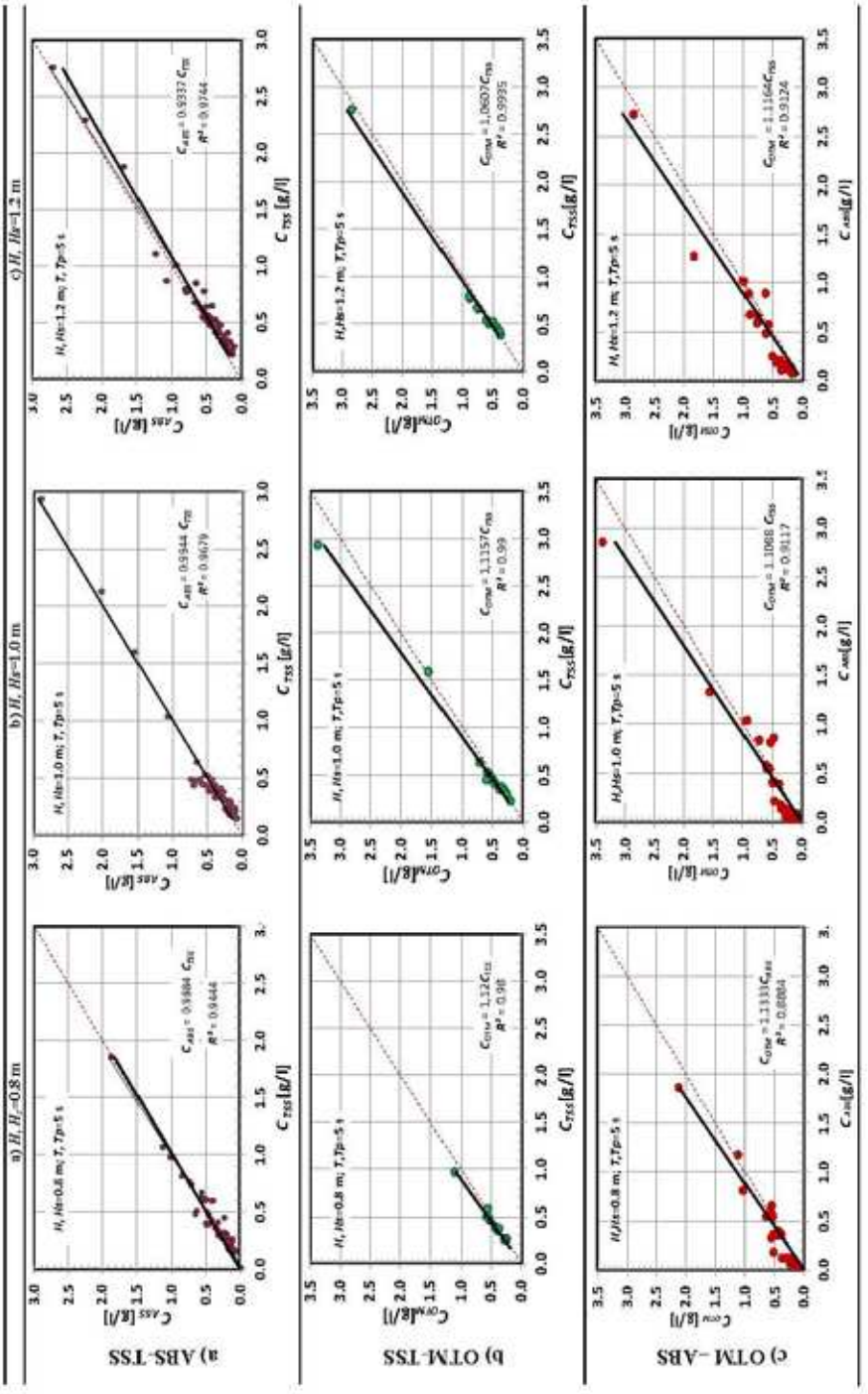

Figure 9 a,b,c: Regression plots between the mean concentrations measured by a) the ABS - TSS, b) the OTM - TSS and c) the OTM - ABS for different wave heights

4.3 Time-dependent measurements

Figure 10 shows the time-varying concentration at four different elevations above the sandy bed measured by the Optical Turbidity Meter (OTM) and the Acoustic Backscatter Sensor (ABS). Figure 10 a indicates the temporal variation of the horizontal component of the free stream intrawave orbital velocity while Figure 10 b shows the variation of the free water surface elevation for a test with a water depth of h=3.18 m; a wave height of H =1.2 m and a wave period of T =5s. Figures 10 c, d, e and f show the time-dependent concentrations at four different levels (the vertical coordinate z is normalised relative to the ripple height η_r; both measured by the ABS) above the ripple crest measured by the ABS (solid black lines) and the OTM (closed circles). A comparison between Figure 10 a and Figures 10 c to f shows that the concentration peaks measured by the ABS and OTM occur approximately at the same phase of the wave cycle. However, the time series of suspended sediment concentration measured by the turbidity meter shows a reasonably steady offset concentration, which is more pronounced at lower heights above the seabed where the concentrations are much higher. This is due to the background turbidity of the relatively fine sediment fractions (silt and mud). This analysis also shows that although the optical device (OTM) and the acoustic device (ABS) were synchronised and mounted in alignment at the measuring station, the time-dependent concentration peaks measured by the optical turbidity meter are slightly ahead in phase compared to the ABS concentration time series (cf. Figures 10 e and f), especially at higher concentration levels. This is an important indication of the fact that the temporal response of the OMT measurement to the wave phase may have suffered a small delay compared to the ABS measurement. This is crucial regarding a precise intrawave analysis of sediment entrainment, especially above ripples, where phase lags between the intrawave flow velocity amplitude and sediment ejection into the water column are highly relevant.

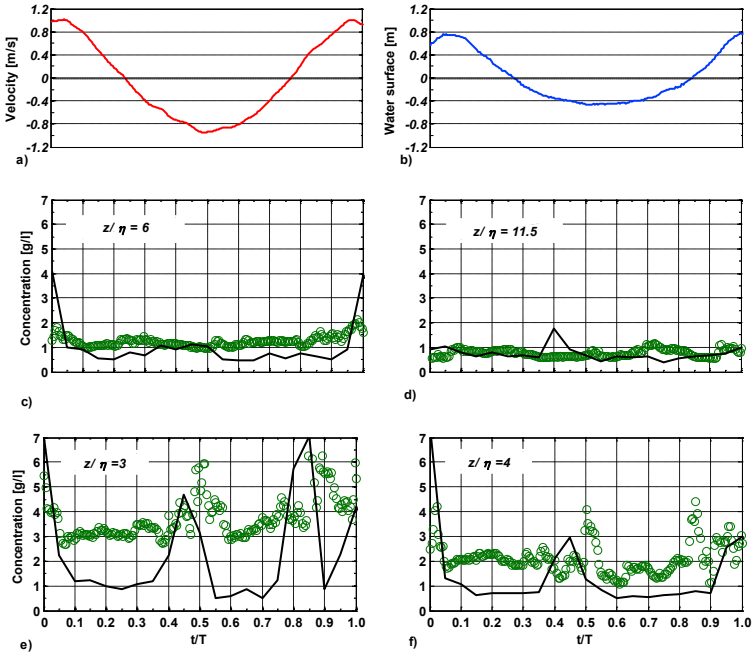

Figure 10: a) Horizontal component of the orbital flow velocity, u, measured at 0.25 m above the seabed. b) Free water surface elevation. c to f) Time-dependent concentrations at different relative elevations z/η_r (η_r ripple height) above the ripple crest measured by the ABS (solid line) and the OTM (circles)

5. Intrawave analysis

Although the measurement and analysis of sediment movement in the nearshore zone have often been undertaken out in recent years, the ability to predict the phenomenon "sediment transport under wave action" is still limited. In particular, the interactive variables of the sediment transport triad and their relative contributions to sediment entrainment mechanisms are not yet sufficiently well-understood (THORNE et al., 2002). Moreover, the considerable number measurements of suspended sediment transport already performed in a rippled bed regime are either time-averaged and bed-averaged or lack sufficient temporal and spatial accuracy. These are the main reasons why past attempts to predict suspended sediment behaviour have severe limitations, especially above steep ripples. The reproduction of suspended sediment events under different hydrodynamic and morphological seabed conditions by means of large-scale laboratory experiments and the correct spatial and temporal analysis of small-scale near-bed sediment processes are therefore crucial to improve our understanding of intrawave sediment transport processes. Measurements of time-dependent suspended sediment concentration were carried out in the present study by means of an ABS. This also included simultaneous measurements of the seabed profile evolution at a fixed measuring station. The results of measurements using the Transverse Suction System (TSS) were also applied to maintain the grain-size profile within the suspension above the seabed as well as to provide mean volumetric concentrations at fixed heights above the seabed. The laboratory tests yielded time-averaged and bed-averaged sediment concentrations obtained using different measuring techniques (see Sec-

tion 3). In this Section, an analysis of detailed small-scale time-dependent suspended sediment concentration events above both rippled and plane seabeds induced by intrawave flow is performed for regular/irregular non-breaking and near-breaking wave.

5.1 Time-dependency of mobile suspended sediment concentrations

Experiments were performed in the Large Wave Flume (GWK) for non-breaking waves, whereby the suspended load above a seabed basically covered by 3-D low-steepness ripples superimposed on 2-D steep vortex ripples represents the dominant transport mode. Due to the decreasing relative water depth over the embankment (near-breaking zone), the waves become asymmetric and finally break. The relatively high near-bed flow energy induced by asymmetric near-breaking waves washes away the steep ripples and the seabed becomes flat just in front of the breaking zone. Figures 11 a and 11 b show a time window of suspended sediment entrainment around a steep vortex ripple (η_r/λ_r = 0.12) under weakly asymmetric non-breaking regular waves (test conditions: H=1.0 m, T= 5s, h/L=0.125) and above a dynamically plane bed (η_r/λ_r = 0) just before the point of wave-breaking under strongly asymmetric near-breaking regular waves (test conditions: H=1.0 m, T= 5 s, h/L= 0.075), respectively. The figures also show the horizontal orbital flow velocity u measured using an Electromagnetic Current Meter (ECM) at a height of 0.25 m above the undisturbed seabed in both cases (given in the 2 panels at the top of Figure 11). The suspended sediment concentrations at different locations beneath the ABS in the bed evolution time series were combined to generate the images.

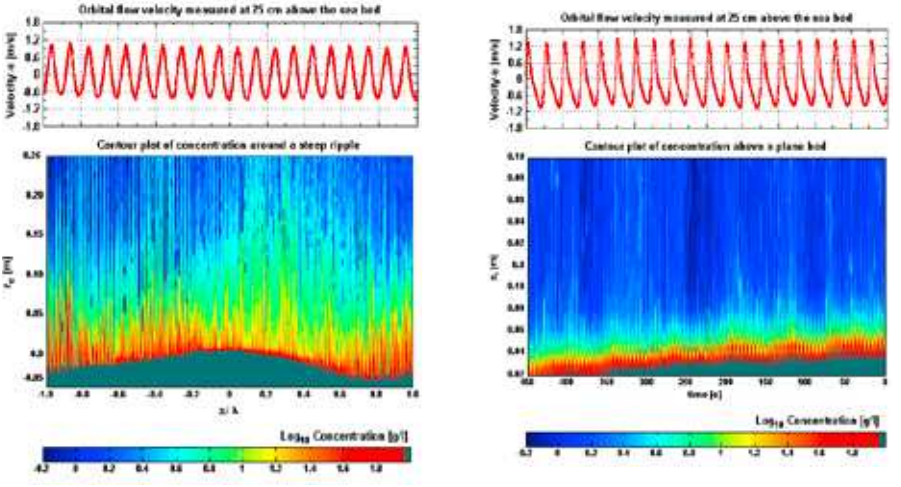

a) SSC above a rippled seabed b) SSC above a plane seabed

Figure 11: Horizontal orbital flow velocity u and Suspended Sediment Concentration (SSC) above (a) a steep ripple beneath weakly asymmetric non-breaking regular waves and (b) a plane bed beneath strongly asymmetric near-breaking regular waves. The colours in the contour plot are defined in the colour bar as "Log 10 (Concentration in g/l)"

5.2 Phase-dependent and bed-dependent concentrations around a steep ripple

In order to investigate the concentration pattern more precisely, random sediment fluctuations must be eliminated. Random fluctuations of flow velocity and bed geometry at the measuring station and in adjacent regions can lead to large scatter and attenuation of the instantaneous concentration measurements. In order to avoid such effects, the velocities measured in successive wave cycles were superimposed to reveal the repeatability of the weakly asymmetrical regular waves during the observation period (phase ensemble averaging). The phase-dependent and ripple-dependent intrawave concentration events above a fully-migrated ripple are discussed by way of example in the following. The observed ripple shown in Figure 12 (η_r/λ_r =0.14) required 700s to migrate completely beneath the ABS, which corresponds to 140 waves with H= 1.2m, T=5s. Panels 1 to 10 of Figure 13 show the corresponding intrawave concentrations measured by the ABS during the wave cycle at each of the 10 equally-spaced numbered points depicted on the seabed profile shown in Figure 12. The suspended sediment concentrations during the entire period (700s; 140 waves) were then ensemble-averaged for the selected points on the migrated ripple (14 successive regular waves corresponding to each point). The horizontal component of the wave-induced orbital flow velocity measured by an ECM at 0.25m above the seabed is shown at the top of Figure 13.

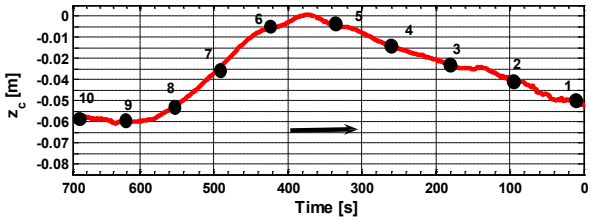

Figure 12: Profile of a fully-migrated ripple beneath the ABS during the measurement period wave conditions: H=1.2m, T=5s, h=3.18m). The arrow indicates the direction of ripple migration

The general concentration peaks are discussed in the following:

- High sediment entrainment is observed on the leeward side of the ripples (locations 1-5 shown in Figure 13; see also Figure 12) between the maximum positive flow velocity and the time of the first flow reversal (around $\varphi = \pi/2$, where $\varphi = \omega t$ is the phase angle).
- With increasing height above the seabed (up to 3 times the ripple height) the concentration peak decreases significantly in magnitude. The sharp drop in the suspended sediment concentration is due to a decrease in the intrawave velocity during the later part of the positive wave half-cycle. Consequently, the developed sediment-laden vortex begins to detach and is entrained at first in the onshore direction ($\pi/4 < \varphi < \pi/2$).
- Two concentration events are observed during the maximum negative wave-induced flow velocity around $\varphi = 2\pi$ and just ahead of the second flow reversal (around $\varphi = 3\pi/2$) on the stoss side of the ripple (locations 6 to 10).

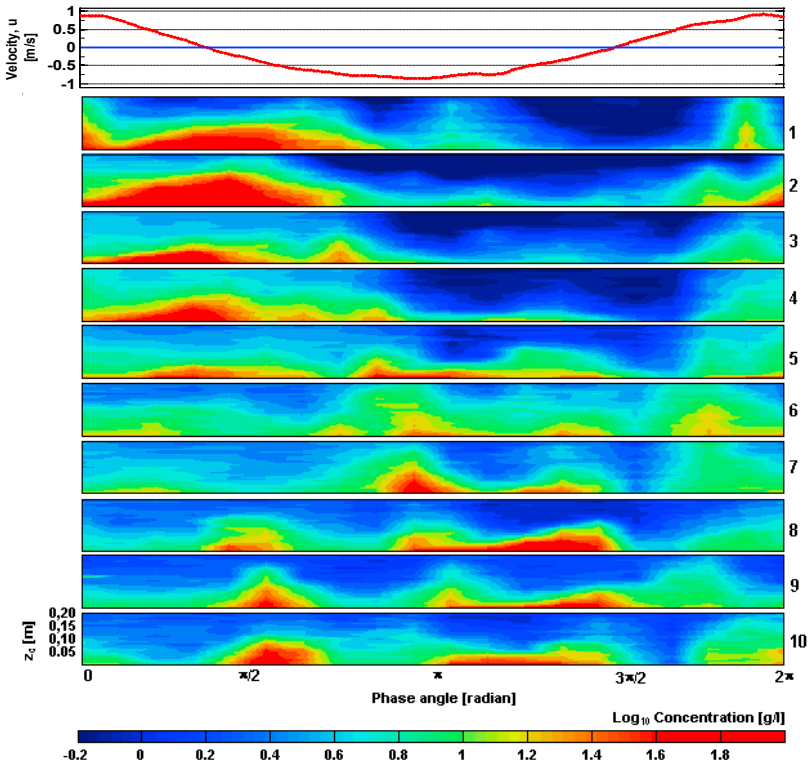

Figure 13: Top panel: horizontal component of the intrawave velocity measured by an ECM at 0.25m above the seabed. Panels 1 to 10: Ensemble phase-dependent and ripple-dependent intrawave suspended sediment concentrations around a steep ripple ($\eta_r/\lambda_r = 0.14$) for the test conducted under 140 successive weakly-asymmetric regular non-breaking waves with H =1.2m T = 5s h =3.18m. The colours in the contour plot are defined in the colour bar as "Log $_{10}$ C", where is the phase-averaged concentration in g/l. The results were obtained in the vertical bins at a height of 0.01m

- The lower peak concentration observed during maximum negative flow conditions indicates the formation of a new vortex on the opposite side of the ripple during the first phase of flow reversal (around $\varphi = 3\pi/2$) due to a lower wave asymmetry compared to the asymmetry generated during maximum positive flow conditions. In contrast to this, the larger peak observed during the negative wave half-cycle on the offshore side of the ripple occurs just ahead of the second flow reversal (around $\varphi = 3\pi/2$), thus indicating shedding of the detached sediment-rich vortex recently generated during the positive wave half-cycle along the onshore slope of the observed ripple.
- Two minor concentration events are observed during the negative wave half-cycle ($\pi/2 < \varphi < 3\pi/2$) on the leeward side of the ripple (locations 1 to 5). These concentration peaks, which occurred after the first flow reversal, indicate that the recently formed sediment clouds on the stoss side of adjacent ripple in the upstream direction roll up towards the observed ripple crest during the period of negatively-directed flow and pass beneath the ABS at the point of insonification at locations 1 to 5.
- During the positive wave half-cycle, secondary low concentration peaks are also observed on the offshore flank of the ripple (locations 6 to 10 shown in Figure 12; ($0 < \varphi < \pi/2$ and $3\pi/2 < \varphi < 2\pi$), which may be explained by the passage of the detached vortices generated by

the adjacent ripple in the downstream direction. These sediment clouds are seen to migrate towards the observed ripple during the remaining period of the positive wave half-cycle and are insonified according to ABS measurements on the opposite side of the ripple.

Examining the phase-averaged concentration panels for all 10 locations (see Figure 13) shows that sediment entrainment around a steep vortex ripple followed by the shedding of detached sediment-laden vortices are coherent in each wave half-cycle within a layer with a thickness of about 3 times the ripple height. Above this layer, the coherent concentration features disintegrate and the diffusion of suspended particles induced by random turbulence seems to be the dominant transport process.

5.3 Phase-dependent ripple-averaged concentrations above a rippled seabed

The above-mentioned two-dimensional analysis shown in Figure 13 yields high-resolution patterns of the complex phenomenon "concentration field around a vortex ripple" within a wave cycle in a two-dimensional vertical (2-DV) domain. This represents a valuable contribution to the quantitative analysis of time-dependent sediment entrainment above the seabed, which in turn helps to improve our understanding of sediment entrainment around a ripple in two dimensions. Due to the complexity of this phenomenon above vortex ripples, however, a two-dimensional analysis of temporal sediment entrainment is very complicated and might not be appropriate for the practical modelling of sediment distribution around steep ripples. In this context, a simpler one-dimensional vertical (1-DV) visualisation (see also DAVIES and THORNE, 2005) is presented in Figure 14, which is obtained by averaging the phase-dependent concentration patterns for the ten locations depicted for the ripple shown in Figure 12 (see also concentration patterns shown in Figure 13). The phase-dependent ripple-averaged concentration field shown in Figure 14 quantitatively visualises the temporal suspended sediment concentration pattern from 1 cm above the ripple crest in the vertical direction up to about 25 cm above the seabed within a superimposed wave cycle. Phase-averaging was repeated for each of the three ABS frequencies and the mean value recorded by two transducers operating at frequencies 1 and 2 MHz was adopted. Due to an excessively wide footprint, the ABS transducer operating at the upper frequency was not taken into consideration in the small-scale intrawave analysis. As illustrated in Figure 14, these results in a phase-dependent ripple-averaged intrawave suspended sediment concentration pattern showing the concentration peaks during a wave cycle. Assuming a horizontally plane seabed on average rather than a rippled surface with a reference level of $z_0 = 1$ cm above the ripple crest, the high-resolution 1-DV concentration pattern shown in Figure 14 confirms that four significant concentration peaks can be clearly identified within a wave cycle, as also observed in Figure 13. The following sedimentary features are evident in Figure 14:

- The largest sediment ejection (peak 1; see Figure 14) occurs around the time of the first flow reversal at $0<t/T<0.4$ ($0<\varphi<16\pi/20$, where $\varphi = \omega t$ is the phase angle). This concentration peak indicates the generation of a lee vortex under the maximum positive velocity of the wave-induced flow in the onshore direction.
- The second concentration peak occurs at $0.4<t/T<0.6$ ($16\pi/20<\varphi<24\pi/20$) under the maximum negative flow velocity. These relatively weak concentration events indicate the

generation of a new low vortex on the stoss side of the ripple under the reversed flow as well as entrainment of the sediment clouds in the offshore direction generated at the adjacent upstream ripple towards the ripple crest during the remainder of the negative wave half-cycle observed on the leeward side of the ripple.

- The third concentration peak occurs at $0.6< t/T <0.8$ ($24\pi/20< \varphi <32\pi/20$). This concentration event takes place just ahead of the second flow reversal and represents the shedding process of the detached sediment-laden vortices generated on the leeward slope of the observed ripple as well as the generation of a minor sediment-laden vortex on the opposite side of the ripple when flow reversal occurs a second time. Due to the asymmetry of the Stokes wave, this concentration peak is smaller, remains close to the ripple and moves over the ripple crest during the next flow reversal (see also Figure 13, panels 6 to 10).
- The fourth concentration peak occurs during the second part of the positive half-cycle after the second flow reversal at $0.8< t/T<1.0$ ($32\pi/20 < \varphi <2\pi$). This concentration peak also indicates the generation of a lee vortex at the observed ripple as well as the onshore migration of the sediment clouds generated at the adjacent downstream ripple and insonified on the stoss side of the ripple.

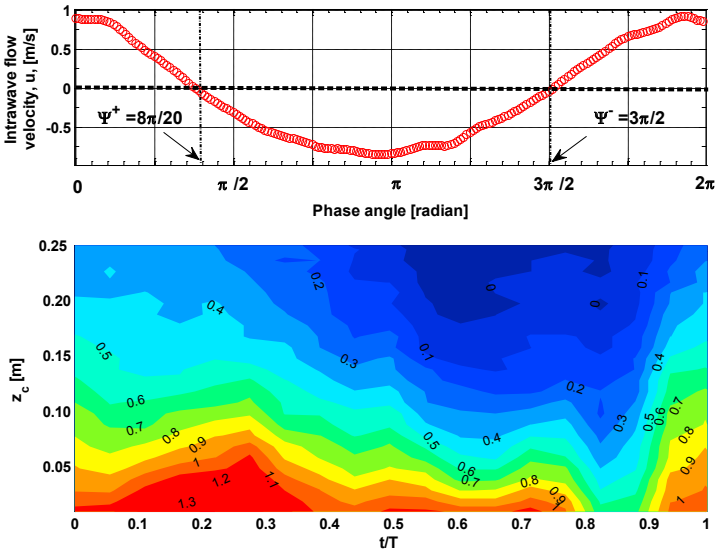

Figure 14: Phase-dependent ripple-averaged ABS concentration pattern (test conditions: H= 1.2 m, T=5 s, h=3.18 m). The numbers on the contour plots are defined as "Log $_{10}$ Concentration" in g/l. The peaks are numbered consecutively from left to right

Based on past observations of intrawave sediment entrainment above rippled seabeds by previous researchers (e.g. DAVIES and THORNE, 2005; THORNE et al., 2003a and b) as well as the observations made in this study, it is concluded that when ripples are steep enough to induce flow separation in the wave bottom boundary layer, sediment entrainment and vortex shedding occur twice during each wave cycle:

- generation of vortices on the ripple sides during the positive and negative wave cycles, respectively, and
- shedding and advection of the detached sediment-laden vortices during the period of flow reversal.

The remainder of the sedimentary events observed in the intrawave concentration patterns (e.g. peaks 2 and 4 in Figure 14) are due to the effects of adjacent ripples (disturbance peaks) and will thus be neglected in the following, which instead concentrates on the intrawave processes during a wave cycle around a given ripple. For more details of sediment entrainment above a rippled seabed, see AHMARI (2012).

5.4 Phase-dependent ripple-averaged concentrations above a plane seabed

Similar to the case of the rippled seabed regime (see Section 5.3 Figure 14), attention is focussed on the phase-dependent bed-averaged suspended sediment concentration profile extending from the seabed surface in the vertical direction up to about 10 cm above the seabed within a superimposed wave cycle. Phase-averaging was repeated for each of the three ABS frequencies to obtain a mean value. The result is illustrated in Figure 15 showing the phase-dependent bed-averaged intrawave suspended sediment concentration pattern. The high-resolution concentration patterns show that immediately before the waves break, when a high-energy flow regime dominates near the bed, (H/L=0.069, h/H= 1.57, U_t/U_c=0.8), the majority of sediment transport occurs in the sheet flow mode within a layer with a thickness of up to 3 cm (with a concentration varying between 3 and 300 g/l). Outside this layer a minor suspended sediment concentration can also be observed, which remains almost constant with height above the seabed and is more pronounced below wave troughs and wave crests. Furthermore, a significant sediment movement event can be observed during the negative wave half-cycle ($0.3<t/T<0.6$) with a peak just before the maximum negative wave-induced flow velocity ($t/T \approx 0.45$). For more details of sediment entrainment above a plane seabed, see AHMARI (2012).

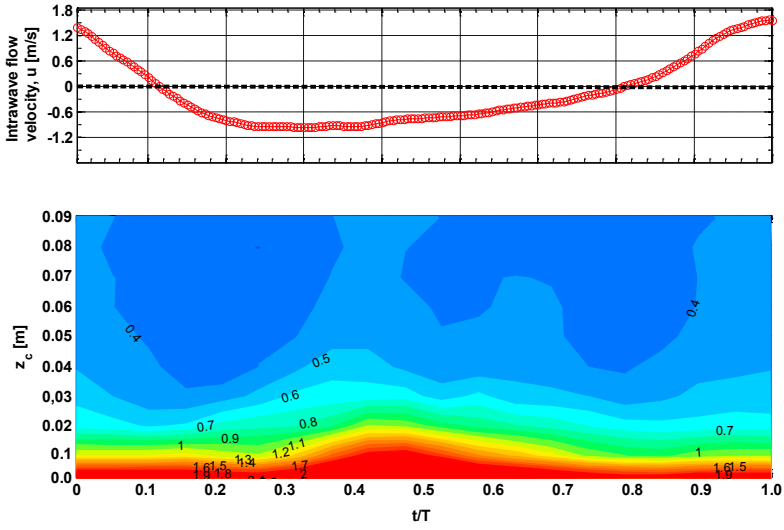

Figure 15: Phase-dependent ripple-averaged ABS concentration pattern (H= 1.0m, T=5s, h/H= 1.57). The numbers on the contour plots are defined as "Log10 Concentration" in g/l

5.5 Effect of sediment diffusivity

5.5.1 Mixing process

As discussed in the previous Sections, an important part of the sediment transport study is to obtain a description of sediment mobilisation and sediment entrainment into the water column induced by the intrawave processes above sandy seabeds. For this purpose, high temporal and spatial resolution can best be achieved using the multi-frequency Acoustic Backscattering System (ABS). In the case of suspended sediment concentration, the turbulent fluctuations in the vertical velocity component intensify the upward mixing process (THORNE et al., 2009). The following equation expresses a balance between the time-averaged vertical turbulent diffusive sediment flux and suspended sediment settling due to gravity:

$$-\varepsilon_s \frac{\partial C}{\partial z} = w_s C \tag{5}$$

where C is the time-averaged sediment concentration, z is the height above the sandy seabed and ε_s is the sediment diffusivity, which is mostly expressed in terms of the turbulent eddy viscosity, ν_t:

$$\varepsilon_s = \beta \nu_t \tag{6}$$

The factor β is either considered to be a constant or is defined by a function involving the suspended sediment concentration and hydrodynamic parameters (e.g. linear, parabolic, exponential or a combination of these). In most studies, however, a linear relation between sediment diffusivity and turbulent eddy viscosity is generally assumed (NIELSEN, 1986; RIBBERINK and AL-SALEM, 1994; VINCENT and OSBORNE, 1993). As mentioned previously, the dominant entrainment processes near a seabed covered with ripples consist in the generation of coherent structures near the ripple surface during the positive wave half-cycle, the detachment of sediment-laden vortices followed by their ejection into the water column, and the advection and shedding of these vortices during the negative wave half-cycle. In contrast to the gradient diffusion solution, in which the mixing length is small compared to the height of the vertical concentration profile based on the description of coherent vortex entrainment, the pure convection concept assumes a mixing length over a relatively larger convective length scale, which is approximately of the same order as the overall scale of the sediment distribution (NIELSEN, 1992). In many circumstances, however, especially under the combined action of waves and currents above a rippled seabed, it is suggested in some recent studies to consider both diffusion and convection processes together (NIELSEN, 1992; THORNE et al., 2002). A detailed understanding of the sediment diffusivity characteristics in both rippled seabed and plane seabed regimes which elucidate the underlying mechanisms leading to the sediment diffusivity distribution and sediment mixing details above the seabed is hence crucial for the development of a reasonable modelling concept. In this context, the ABS concentration measurements were used to determine sediment diffusivity. In the following, this method is used to calculate and analyse the sediment diffusivity characteristics under two distinct conditions:

- above a rippled seabed under the action of weakly asymmetric non-breaking waves and
- above a plane bed under the action of strongly asymmetric near-breaking waves.

DAVIES and THORNE (2008) introduced a modelling framework to classify the turbulent oscillatory flows above natural bed structures which is dependent on:

- the wave Reynolds number, $\mathrm{Re_A} = \mathrm{AU}/\nu$, where A is the orbital amplitude, U is the amplitude of the near-bed flow velocity and ν is the eddy viscosity,
- the relative roughness, $\mathrm{A}/\mathrm{k_s}$, where $\mathrm{k_s}$ is the equivalent bed roughness and
- the peak Shields parameter, $\hat{\theta} = \hat{\tau}/\left\{\left((\rho_s/\rho)\text{-}1\right)\mathrm{gd_{50}}\right\}$, where $\hat{\tau}$ is the peak bed shear stress, ρ_s and ρ are the densities of the sediment and water, respectively and $\mathrm{d_{50}}$ is the median grain diameter.

Table 6 gives a comparison between bed form characteristics associated with the wave Reynolds number ($\mathrm{Re_A}$) calculated here from the test data and suggested by DAVIES and THORNE (2008). According to this classification, well-developed steep vortex ripples (long-crested, two-dimensional ripples) occur in a "low energy flow" regime, where $\mathrm{Re_A} = \mathrm{O}(10^3\text{-}10^4)$; $\mathrm{A_0}/\mathrm{k_s} = \mathrm{O}(1)$ and $0.05 \leq \hat{\theta} \leq 0.2$). A comparison between this classification and the values calculated for the experiments in test groups 1 and 2 (see Table 6) shows that the tests were performed under conditions ranging between the "upper level" of the low energy flow condition to the transitional condition.

Table 6: Bed form characteristics associated with the wave Reynolds number (Re)

	After Davies and Thorne (2008)		**Calculated for the tests above ripples (Test group 1 and 2)**
	2D steep ripples	**2D and 3D low ripples**	
	Low energy conditions	**Transitional conditions**	
Re_A	$O(10^3 - 10^4)$	$O(10^4 - 10^5)$	$O(10^5)$
A_0/k_s	$O(1)$	$O(1 - 10)$	2-30
$\hat{\theta}$	$0.05 \leq \hat{\theta} \leq 0.2$	$0.2 \leq \hat{\theta} \leq 0.6$	0.3-0.6

As can be seen in Table 6, the hydrodynamic conditions dominant in test groups 1 and 2 approach the upper limit of the transitional condition suggested by DAVIES and THORNE (2008). Consequently, the ripples observed in the tests performed in the present study are somewhat lower than those observed by Davies and Thorne. The general form of the ripples generated in the wave flume during the tests has already been extensively discussed in Section 3.4. Here it was shown that they mostly tend to resemble two and three-dimensional less steep ripples superimposed on individual 2-D vortex ripples, which occasionally appear and migrate in the onshore direction beneath the ABS. In Sections 5.2 and 5.3 it was also shown that the leeward side of the generated ripples contributes to the periodic vortex generation process. In this connection, the vertical component of the periodic wave-induced near-bed orbital flow velocity, $\mathrm{w_w}$, should significantly dominate the vertical upward sediment flux $\overline{\mathrm{w_w C_p}}$ near the seabed, where $\mathrm{C_p}$ is the periodic suspended sediment concentration. Taking account of the fact that the sediment diffusivity is defined by the vertical turbulent sediment flux $\overline{w'c'}$, the time-averaged sediment balance above the ripples may be expressed as follows (THORNE et al., 2009):

$$-w_s C + \overline{w_w C_p} - \varepsilon_s \frac{dc}{dz} = 0 \tag{7}$$

where the sediment diffusivity is given by:

$$\varepsilon = \frac{-w_s C}{dC/dz} \tag{8}$$

In this context, the ABS measurements of suspended sediment concentration were additionally taken into consideration. Using the vertical distribution of the mean grain size, $d_{50,s}$, (black line; Figure 16) determined from TSS measurements near the seabed (three angles in Figure 16) and predicted at higher elevations based on previous measurements by THORNE et al. (2009) (red circles; Figure 16) and BLACK (1994) (rectangles; Figure 16), it is possible to calculate the time-averaged vertical profile of the settling velocity, w_{sc}, according to SOULSBY (1997) as follows:

$$w_{sc} = \frac{\upsilon}{d_{50s}}\left[(10.36^2 + 1.049(1-C)^{4.7}\, D_*^3)^{0.5} - 10.36\right] \tag{9}$$

where D_* is the dimensionless grain size:

$$D_* = d_{50}\left[\frac{(s-1)g}{\upsilon^2}\right]^{1/3} \tag{10}$$

In the above, s represents the grain to water density ratio (ρ_s/ρ); g the acceleration due to gravity and υ the kinematic viscosity. However, the effect of settling velocity, w_{sc}, has only be taken into consideration at very high concentration levels (C >130 g/l within a few millimetres above the seabed). Above this very thin layer, no significant variation of the settling velocity with height above the seabed has yet been reported. According to SOULSBY (1997), the difference between w_{sc} and w_{sc} for smaller concentrations (outside the thin high-concentration layer close to the seabed) is less than 20%. This means that the settling velocity, w_s, may be written as follows:

$$w_s = \frac{\upsilon}{d_{50s}}\left[(10.36^2 + 1.049\, D_*^3)^{0.5} - 10.36\right] \tag{11}$$

Furthermore, an examination of the suspended sediment grain-size distribution illustrated in Figure 16 a shows that the suspended sediment particles at higher elevations are much smaller than those near the sandy seabed $d_{50,s}/d_{50,b} = 45.5\%$; $d_{50,s}$ represents the grain size in suspension and $d_{50,b}$ the same near the seabed). Moreover, Figure 16 b shows by way of example the time- and bed-averaged vertical profiles of suspended sediment concentration measured by the ABS under the action of both regular and irregular waves, which were used to calculate the time-averaged sediment diffusivity in both regular and irregular wave regimes.

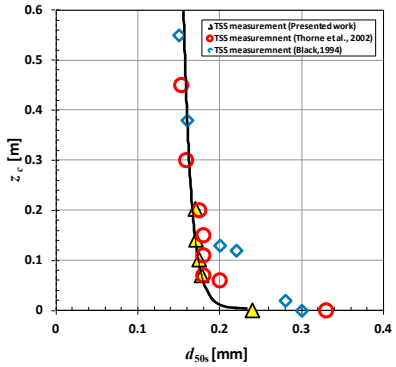

d50-distribution (TSS data)

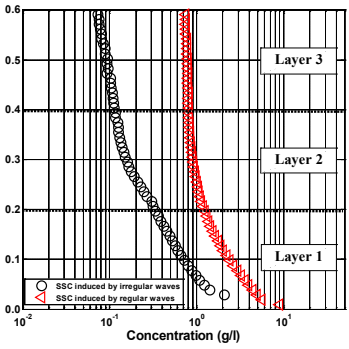

b) SSC distribution (ABS data)

Figure 16: Distribution of (a) suspended sediment size d_{50S} (red circles) at different heights z above the seabed. The vertical distribution of the mean grain size (black line) is fitted to the TSS measured data. The red circles represent the suspended particle diameter, d_{50S}, measured by Thorne et al. (2002) at different heights above the seabed and the rectangles represent the suspended sediment size (d_{50S}) above the seabed after Black (1994) and (b) suspended sediment distribution (SSC) induced by regular waves and measured by the ABS (H=1.2m, T=5s; black circles) and irregular waves (H_s=1.2m, T_p=5s, γ =3.3; red triangles)

5.5.2 Sediment diffusivity above rippled beds

Figures 17 a and b show the sediment diffusivity profiles for 30 experiments involving irregular waves (test conditions: H_s=0.8-1.2m, T_p= 5s, γ=1.0- 9.9, h=3.17-3.21m) and 18 experiments involving regular waves (test conditions: H=0.8-1.2m T=5s and h= 3.15-3.23m), respectively (test group 1, see Figure 2). The grey points represent the calculated sediment diffusivity profiles at different heights above the seabed, whereas the red circles show the averaged values for the case of irregular and regular waves, respectively. In qualitative terms, the vertical distribution of the time-averaged sediment diffusivity induced by regular and irregular waves can be considered in three different layers:

- **Layer 1 (z < 20 cm; low sediment diffusivity):** In both regular and irregular wave regimes, a nearly constant sediment diffusivity is observed. This indicates the effect of coherent structures around the ripples.
- **Layer 2 (20 cm < z < 40 cm; transitional zone):** The sediment diffusivity increases linearly with height initially above the seabed. The SSC gradient ($\partial c/\partial z$) induced by irregular waves is more pronounced than that below regular waves.
- **Layer 3 (40 cm < z; high sediment diffusivity):** The gradient of the linear increase in sediment diffusivity gradually decreases until an approximate maximum value is attained. The large scatter in the vertical profiles evident at greater heights above the seabed is due to the inherently noisier lower concentrations at higher elevations in the water column (THORNE et al., 2009).

Within the first layer (z < 20 cm), sediment diffusivity is seen to be small ($\varepsilon_s \approx 0.001$ m²/s) due to a sharp decrease in sediment concentration within a few centimetres above the ripple crest (high values of $\partial c/\partial z$). As can be seen in Figure 17 a and b, this small value of sediment diffusivity remains constant with height above the seabed. This is due to the constant decrease in suspended sediment concentration (cf. Figure 17 b) related to the coherence of vortex generation processes that occur close to the rippled seabed. Above this layer (20 cm < z <40 cm), the coherent structures break

down and momentum transfer takes place by random turbulence, which increases linearly with height above the seabed. A linear increase in sediment diffusivity based on a constant linear decrease in the mean vertical suspended sediment concentration distribution can clearly be seen within layer 2.

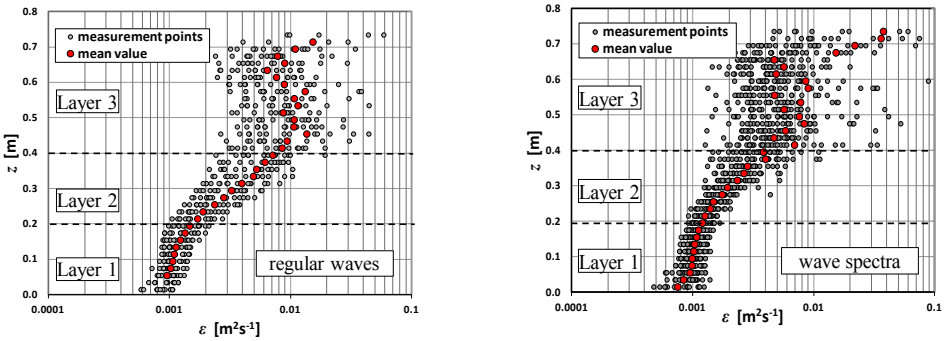

a) Diffusivity profile beneath regular waves

b) Diffusivity profile beneath irregular waves

Figure 17: Sediment diffusivity profiles at heights z above the seabed beneath (a) regular waves (H=0.8-1.2m, T=5s, h=3.15-3.23m) and (b) irregular waves (H_s= 0.8-1.2m, T= 5s, γ =1- 9.9, h=3.17-3.21m). Grey points represent the measured sediment diffusivities with height above the seabed while the red points indicate the mean values of the plotted points at the corresponding heights

Furthermore, a comparison between Figure 17 a and Figure 17 b shows that the sediment diffusivities beneath regular waves (graph a) are somewhat greater than the diffusivity values beneath irregular waves (graph b) at the same heights above the seabed. This effect is more pronounced within layer 2, which indicates that momentum transfer induced by regular waves is greater at higher elevations than for irregular waves. As discussed in Section 4.2, the suspended sediment concentration distribution under the action of both regular and irregular waves decreases exponentially. However, at higher elevations above the seabed (z>20 cm), both the magnitude of the suspended sediment concentration and the distribution gradient $(\partial c/\partial z)$ decrease drastically. Within layer 2 for regular waves, the suspended sediment concentration event approximately attains a constant value, thereby resulting in larger values of sediment diffusivity compared to those obtained under irregular wave conditions (cf. Figure 16 b). However, the increase in sediment diffusivity at higher elevations is more obvious up to about 40 cm above the averaged seabed level (within level 2; the transitional layer). Despite the inherent scatter in the ABS measurements at higher elevations (z> 40 cm; layer 3; the region of low concentrations), the mean sediment diffusivity tends to approximately attain a maximum value of about 0.01 m²/s for both regular and irregular waves (see Figure 17 a and b). Furthermore, the mean grain size in suspension ($d_{50,s}$) also decreases and becomes almost constant at higher elevations (see Figure 16 a). Therefore, based on the very low concentration gradient ($\partial c/\partial z \rightarrow 0$) and almost uniform gradient of suspended grain-size ($\partial d_{50,s}/\partial z \rightarrow 0$), the sediment diffusivity tends to attain a maximum and remains constant with height above the seabed within layer 3 (upper concentration level) (cf. Equation 8). Due to the large scatter, however, the measurement points in layer 3 are not representative enough to indicate a clear trend for the mean sediment diffusivity distribution at higher levels (z>40 cm) (Figure 17 a and b). Owing to a very rapid decrease in the suspended sediment concentration with height above the seabed at higher elevations, however, the sediment diffusivity decreases drastically towards the water surface and the general form of the

vertical distribution of averaged sediment diffusivity becomes parabolic (see Figure 18). The parabolic form of the time-averaged wave-induced eddy viscosity $\overline{\nu}_t$, with distance from the bed has also been reported by previous researchers (NIELSEN, 1992; GARCIA, 2007; MARGVELASHVILI, 2003) (see also AHMARI, 2012). Figure 18 a and b show the variation of mean sediment diffusivity (black line in graph b) based on the vertical distribution of suspended sediment concentration (red line in graph b) related to the height above the seabed (z). As explained in the table on the left (Figure 18-a), due to the action of the coherent structures and the high suspended sediment concentration gradient ($\partial c/\partial z$) in the first layer (ca. 20 cm) above the seabed, the sediment diffusivity is minimum and almost constant above the seabed. Within the second layer, the coherent sediment-laden vortices disintegrate and momentum transfer takes place by random turbulence. As is clearly evident in the figure, the suspended sediment concentration gradient decreases compared to the first layer and the mean sediment diffusivity increases almost linearly. Additionally, the mean suspended sediment concentration, C, is still high within layer 2 compared to the concentrations at higher elevations. This means that the decrease in the suspended sediment gradient ($\partial c/\partial z$) is greater than that of the suspended sediment concentration itself. Above Layer 2, a balance seems to occur between the reduction in the concentration gradient ($\partial c/\partial z$) and the reduction in the absolute magnitude of the mean suspended sediment concentration ($\overline{C}$). This leads to a maximum value of sediment diffusivity at this height above the seabed (maximum diffusivity of suspended sediment, ε_{max}). Due to a sharp decrease in the mean concentration at higher elevations (above layer 3), the mean sediment diffusivity profile decreases drastically towards the water surface.

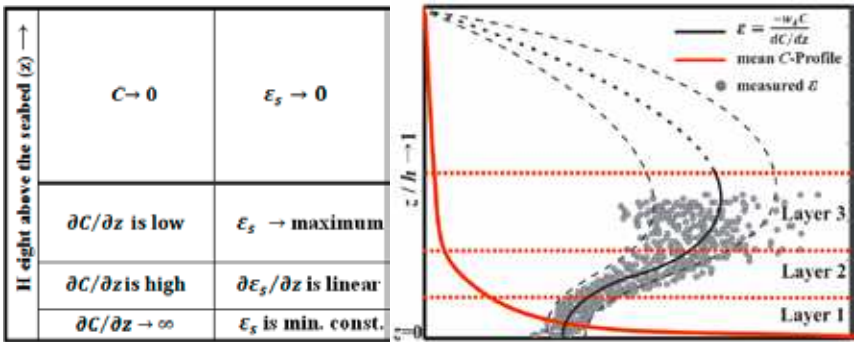

a) Variation of ε_s and SSC with height (ε_s)

b) ε_s and mean $\overline{C}$-profile with height above a rippled seabed (z)

Figure 18: Variation of mean sediment diffusivity (black line; graph b) based on the mean suspended sediment concentration profile (red line; graph b) related to the height above a rippled seabed (z)

In order to represent the trends in sediment diffusivity and assess the consistency of the results given by different approaches, the sediment diffusivity profiles were normalised using the four most frequently applied scaling procedures adopted in previous research studies given by THORNE et al. (2009), including the mean values for each case as follows:

$$\left.\begin{array}{l} \text{a) } \varepsilon_s/\kappa\overline{u}_*h \text{ with } z/h \\ \text{b) } \varepsilon_s/\kappa\overline{u}_*\delta_w \text{ with } z/\delta_w \\ \text{c) } \varepsilon_s/U\eta_r \text{ with } z/\eta_r \\ \text{d) } \varepsilon_s/Uk_s \text{ with } z/k_s \end{array}\right\} \quad (12)$$

with

$$\overline{u}_* = 0.763(f_w/2)^{0.5}U \quad (13)$$

$$f_w = 0.237\left(\frac{k_s}{A_0}\right)^{0.52} \quad (14)$$

$$\delta_w = \overline{u}_*/\omega \quad (15)$$

where δ_w is the scale thickness of the wave boundary layer; $\overline{u}_*$ the mean friction velocity; U the wave-induced flow velocity amplitude just above the wave bottom boundary layer; ω the radian frequency; f_w the friction factor; η_r the ripple height; z the height above the ripple crest; h the water depth; and Karman's constant, $\kappa = 0.4$. According to the suggestion proposed by THORNE et al. (2002, 2009), the equivalent bed roughness k_s for a rippled seabed is taken as follows:

$$k_s = 25\eta_r(\eta_r/\lambda_r) \quad (16)$$

where λ_r is the ripple length and η_r the ripple height. According to THORNE et al. (2009), Equation (16) represents the convective contribution to the upward mixing of momentum and sediment more precisely than the relation suggested by NIELSEN (1992), in which $k_s = 8\eta_r(\eta_r/\lambda_r)$. Figure 19 shows the results of the normalised data for the tests over a rippled seabed under the action of regular waves (H= 0.8-1.2m, T=5s, $h \approx$ 3.18m). The grey dots represent the sediment diffusivities measured in each test and the dark dots, the averaged profile for each normalisation. As can be seen in Figure 19 a,b,c and d, all four normalisations clearly show a common trend in the sediment diffusivity profiles, as is also evident in Figure 17 a and b. The three identified layers for the sediment diffusivity profiles depicted in Figure 17 can also be recognised in all normalised plots in Figure 19. The normalisations given in Figure 19 show how the normalised sediment diffusivity remains almost constant at a low value with relative height above the seabed within layer 1, increases linearly with relative height within layer 2 and tends to approach a constant high value with normalised height above the seabed within layer 3. The averaged profile of sediment diffusivity in each normalisation takes on the form of the normalised sediment diffusivity with relative height above the seabed in the rippled seabed regime, as is also evident in the sediment diffusivity profiles before normalisation (see Figure 17). THORNE et al. (2009) considered the normalisation given by Equation (12 d) (see Figure 19 d) as a final result to describe sediment diffusivity above ripples mathematically. In this study the same normalisation is adopted to permit possible comparisons with the results of THORNE et al. (2009).

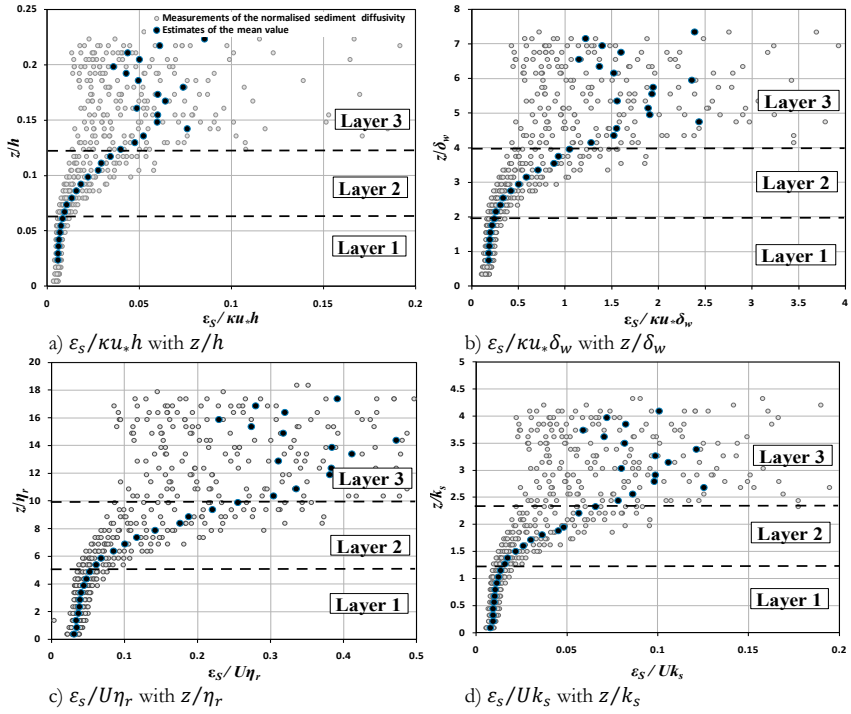

a) $\varepsilon_s/\kappa u_* h$ with z/h b) $\varepsilon_s/\kappa u_* \delta_w$ with z/δ_w

c) $\varepsilon_s/U\eta_r$ with z/η_r d) ε_s/Uk_s with z/k_s

Figure 19: Normalised sediment diffusivities vs. normalised height above a rippled seabed under the action of regular waves (H= 0.8-1.2m, T=5s, $h \approx$ 3.18m)

5.5.3 Interpretation of the sediment diffusivity profiles and empirical prediction formulae

Figure 20 shows comparisons of averaged sediment diffusivities (ε_s/Uk_s) with height above the seabed (z/k_s). Figure 20 a shows mean sediment diffusivity profiles whereas Figure 20 b shows normalised mean sediment diffusivity profiles. The profiles plotted with blue circles are for regular waves (H= 0.8 – 1.2 m, T=5 s, h=3.20 m) while those plotted with red circles are for irregular waves (JONSWAP-spectra with H_s=0.8–1.2 m, T_p=5s, h= 3.18 m, γ=1.0-9.9). As is evident in the figure, there are no significant differences between the two cases within layer 1, which extends from the seabed to a normalised height of z/k_s= 1.2 above the seabed. Within layer 1, the normalised sediment diffusivity remains almost constant ($\varepsilon_s/Uk_s \approx$ 0.01) beneath both regular and irregular waves. Above this height (layer 2), the averaged sediment diffusivity increases linearly in both cases. As discussed above, the mean sediment diffusivity generated beneath regular waves is significantly greater than beneath irregular waves at each height level in layer 2.

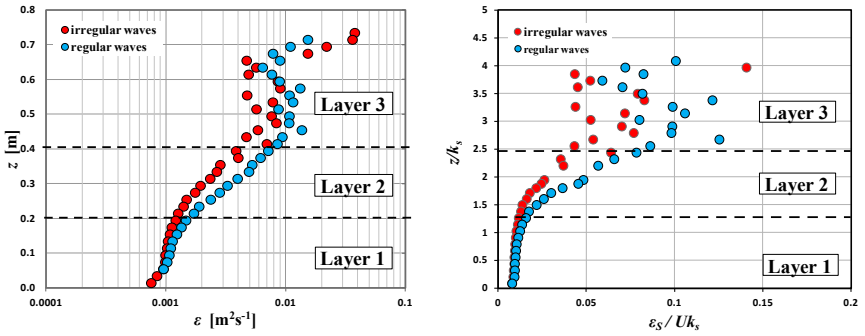

a) mean sediment diffusivity profiles b) normalised mean sediment diffusivity profiles

Figure 20: Comparison between mean sediment diffusivity profiles above a rippled seabed calculated for irregular waves (red circles) (H=0.8, 1.0, 1.2m; T=5s) and regular waves (blue circles) (H_s=0.8, 1.0, 1.2 m ; T_p=5s; γ=1.0-9.9); (a) mean sediment diffusivity profiles and (b) normalised mean sediment diffusivity profiles

Although the behaviour of the mean sediment diffusivity distribution becomes less clear at higher elevations ($z/k_s > 2.5$), a maximum value is distinctly recognisable at the top of layer 2. Empirical expressions were finally fitted to the mean sediment diffusivity profiles within layers 1 and 2 for both sets of measurements beneath regular and irregular waves (Figure 21 a and b; up to 40 cm above the seabed), respectively, to describe the variation of sediment diffusivity with height above the seabed. Due to the high attenuation in concentration measurements at higher elevations, the derivation of a clear expression to describe the mean distribution of measured diffusivities in layer 3 is hardly possible.

- Beneath regular waves (Figure 21 a)

$$\varepsilon_s = \xi_1 U k_s \qquad z \leq 1.2 k_s \tag{17}$$

$$\varepsilon_s = \xi_2 U (z - k_s) \qquad 1.2\, k_s < z < 2.5 k_s \tag{18}$$

where $\xi_1 = 0.0112$, $\xi_2 = 0.06$.

- Beneath irregular waves (Figure 20 b):

$$\varepsilon_s = \xi_1 U k_s \qquad z \leq 1.5 k_s \tag{19}$$

$$\varepsilon_s = \xi_2 U z - \xi_3 U k_s \quad 1.5 k_s < z < 2.5 k_s \tag{20}$$

where $\xi_1 = 0.0112$, $\xi_2 = 0.039$ and $\xi_3 = 0.047$

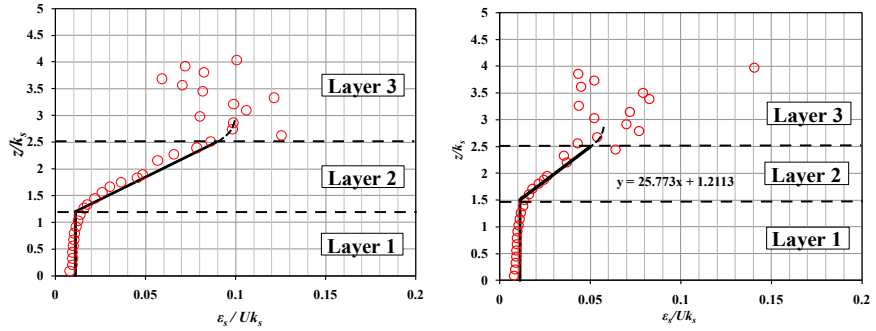

a) Beneath regular waves b) Beneath irregular waves

Figure 21: Mean measured normalised sediment diffusivity above a rippled seabed induced by non-breaking waves. a) beneath regular waves, b) beneath irregular waves

Furthermore, Figure 21 a and b clearly illustrate the constant form of the sediment diffusivity profiles up to $z = 1.2\ k_s$ above the seabed in the case of regular waves and $z = 1.5\ k_s$ in the case of irregular waves. Taking into account the fact that the absolute height of the area in which the sediment diffusivity is constant is approximately $z = 20$ cm in both regular and irregular wave regimes (see Figure 17 a and b), it can be concluded that the equivalent roughness, k_s, above a rippled seabed is approximately:

$$k_s \approx 2.6\eta_r \text{ under irregular waves and}$$

$$k_s \approx 3\eta_r \text{ under regular waves} \quad (21)$$

Table 7 comparatively summarises the empirical formulae for sediment diffusivity determined in previous studies. The measurements beneath regular waves performed by THORNE et al. (2009) suggest that sediment diffusivity remains almost constant close to the ripple surface (layer 1 shown in Figure 21). This may be explained by the action of coherent structures (gradient diffusion) in a layer with a thickness of almost three times the ripple height ($3\eta_r$). Due to disintegration of the well-organised coherent structures at higher elevations (layer 2 in Figure 20), sediment diffusivity is no longer constant but increases linearly with height above the seabed. Considering the formulations for sediment diffusivity within layer 1 suggested by NIELSEN (1992) and VAN RIJN (1993), the value predicted by Nielsen's formulation (ε_s=0.016 Uk_s) is much closer to the value determined in the presented study (ε_s=0.0112 Uk_s) than the value calculated on the basis of Van Rijn's suggestion, which is very close to the near-bed sediment diffusivity obtained by THORNE et al. (2009) (ε_s=0.029 Uk_s). The discrepancy in relative sediment diffusivities in different test series can be explained by the fact that the mean grain size used in the present study (d_{50b}=0.24 mm) was about 30% smaller than that used by THORNE et al. (2009) (d_{50b}=0.33 mm). Taking into account that the heavier the sediment particles are then the larger is the settling velocity, the mean sediment diffusivity will consequently be smaller in the case of finer sand (see Equation 11). Furthermore, the different hydrodynamic conditions under which tests were carried out in the different studies (e.g. water depth, wave heights, wave periods and wave asymmetry) account for different ripple steepnesses, different

periodic shear stresses, $\tilde{\tau}$, velocity gradients ($\partial u/\partial z$), momentum transfer and consequently, different wave-induced turbulent eddy viscosities, ν_t,, above the seabed.

Table 7: Summary of empirical prediction formulae for sediment diffusivity above rippled beds

	Formulations	Parameter	Remarks
NIELSEN (1992)	$\varepsilon_s = \xi_1 U k_s$	$\xi_1 = 0.016$ $k_s = 8\eta_r(\eta_r/\lambda_r)$	Near bed sediment diffusive (regular waves)
VAN RIJN (1993)	$\varepsilon_s = \alpha_b U k_s \quad (z \le \zeta_s)$ $\varepsilon_m = \alpha_m \frac{Hh}{T}$	$\zeta_s = 3\eta_r$ (thickness of the near bed mixing layer) $\alpha_b = 0.004 D_*$ $D_* = d_{50}[(s-1)g/\upsilon^2]^{1/3}$ α_m =0.035	ε_s: Sediment diffusivity near the seabed ($z \le \zeta_s$) ε_m: Eddy viscosity in the upper layer (regular waves)
LEE et al. (2002)	$\varepsilon_s = \beta\kappa\bar{u}_* z$	$\bar{u}_* = 0.763(f_w/2)^{1/2} U$ $f_w = 0.237\left(\frac{k_s}{A_s}\right)^{0.52}$ $\kappa = 0.4$	Linear increase in ε_s with the height above the seabed (regular and irregular waves)
THORNE et al. (2009)	$\varepsilon_s = \xi_1 U k_s$; $(0 < z \le 1.3k_s)$ $\varepsilon_s = \xi_2 U z - \xi_3 U k_s$ $(z > 1.3k_s)$	$\xi_1 = 0.029$ $\xi_2 = 0.028$ $\xi_3 = 0.007$ $k_s = 25\eta_r(\eta_r/\lambda_r)$	Sand size d_{50}=330 µm; Under regular waves: (H=0.5 and 0.8 m) (T=5 s and h≈4.5m)
AHMARI (2012)	$\varepsilon_s = \xi_1 U k_s \quad (0 < z \le 1.2k_s)$ $\varepsilon_s = \xi_2 U(z - k_s)$ $(1.2\ k_s < z < 2.5k_s)$	$\xi_1 = 0.0112$ $\xi_2 = 0.06$ $k_s = 25\eta_r(\eta_r/\lambda_r)$	Sand size d_{50}=242 µm; Under regular waves (H=0.8, 1.0, 1.2 m) (T=5 s and h≈3.2m)
AHMARI (2012)	$\varepsilon_s = \xi_1 U k_s \ (0 < z \le 1.5k_s)$ $\varepsilon_s = \xi_2 U z - \xi_3 U k_s$ $(1.5\ k_s < z < 2.5k_s)$	$\xi_1 = 0.0112$ $\xi_2 = 0.039$ $\xi_3 = 0.047$ $k_s = 25\eta_r(\eta_r/\lambda_r)$	Sand size d_{50}=242 µm; Under irregular waves (H_s=0.8, 1.0, 1.2 m) (T_p=5 s and h≈3.2m)

Within layer 1 close to a rippled seabed ($z/k_s < 1.2$ for irregular wave conditions and $z/k_s < 1.5$ for regular wave conditions; see also Figure 5.10 and Table 5.3), the following conclusions may be drawn:

- under low to transitional energy flow conditions involving fine to medium sand, the empirical formula given by NIELSEN (1992) seems to yield a better prediction of sediment diffusivity within the near ripple layer, whereas
- under low energy flow conditions above coarse sand, the formulation of VAN RIJN (1993) appears to be more applicable.

Table 8: Summary of the test conditions for tests performed by THORNE et al. (2009) and for tests performed in this study

Experiments	Bed Material	Grain Size [μm]			H, H_s [m]	T, T_s [s]	H [m]	Bed Form
		d_{10}	d_{50}	d_{90}				
THORNE et al. (2009)	medium to coarse sand	170	330	700	0.6 - 1.1	4-6	4.5	"well developed 2D Steep Ripples" $\eta_r/\lambda_r = 0.14,\ \hat{\theta} < 0.2$ $A/k_s = O(1)$ $Re = O(10^3 - 10^4)$
	fine sand	95	160	300	0.5 - 1.1	4-6	4.5	"Dynamically plane bed" $\eta_r/\lambda_r = 0.07,\ \hat{\theta} > 0.7$ $A/k_s = O(100 - 1000)$ $Re = O(10^6 - 10^7)$
AHMARI (2012)	fine to medium sand	125	242	470	0.8 1.0	7, 5	3.2	"2D and 3D ripples" $\eta_r/\lambda_r > 0.12,\ \hat{\theta} < 0.7$ $A/k_s = 2 - 30$ $Re = O(10^5 - 10^6)$

Considering the value of constant sediment diffusivity above a rippled seabed predicted by Nielsen's formula (ε_s=0.016 Uk_s) in layer 1, good agreement is obtained between this prediction and the sand diffusivities determined in this study for both regular and irregular waves. Within er 2 ($1.2\ k_s < z < 2.5k_s$ for regular waves; $1.5\ k_s < z < 2.5k_s$ for wave spectra), the sediment diffusivity distribution is no longer constant but increases linearly with height above the seabed. This is verified by the averaged sediment diffusivities measured by THORNE et al. (2009) and the diffusivities measured in this study as well as the values predicted by the formulae of VAN RIJN (1993) and LEE et al. (2002). For further details of sediment diffusivity and sediment diffusivity above plane seabeds see AHMARI (2012).

6. 1DV model for suspended sand concentrations above rippled seabeds

As mentioned in Section 2.4, a number of modelling techniques are available for predicting time-averaged and time-dependent sediment transport in terms of suspended load, bed load or sheet flow under different steady and unsteady flow regimes, which, according to NIELSEN (1992), may be subdivided into two main groups:

- $C * u$ integrated models: concentration times velocity integral.
- Particle trajectory models: time-averaged pick-up range times the average distance travelled by sediment particles.

From the practical point of view, it is important to be able to predict the suspended sediment flux above vortex ripples (magnitude and transport direction), which constitutes a major part of the total time-averaged and time-dependent sediment transportation in the nearshore zone. Further details of the latter are discussed in the following.

6.1 Time-dependent suspended sediment concentrations

When waves propagate towards the shoreline, the hydrodynamic regime changes along the beach profile (AHMARI, 2012). These changes result in different bed forms, which in turn modify the structure of the wave bottom boundary layer and thus the mechanism of near-bed sediment entrainment. As extensively discussed in Section 5.2, flow separation on steep ripple crests contributes to the separation of the wave bottom boundary layer and consequently to an enhancement of sand particle entrainment around the ripples by the generation of lee vortices, which are brought into suspension by the shedding process at times of flow reversal. In fact, the time-dependent suspended load represents a more significant transport mode above a rippled seabed than above a plane seabed. Moreover, due to the absence of steep ripples on plane seabeds and for higher near-bed flow energy, the dominant sediment transport mode is sheet flow. The extensive analysis of the observations of intrawave sediment concentration distributions above a rippled seabed given in Section 5 has shown that the coherent sediment dynamics induced by forcing hydrodynamics around a steep ripple can be subdivided into three distinct mechanisms:

- Flow separation and vortex generation: generation of vortices under positive and negative flow conditions on the leeward side of steep ripples.
- Sediment entrainment: detachment of fully-developed sediment-rich vortices from the ripple surface.
- Sediment-laden vortex shedding: advection of detached sediment-laden vortices during flow reversal to higher elevations above the seabed followed by shedding processes in the onshore and offshore directions.

While the bed shear stress concept applies well to a description of sediment motion on the seabed due to the contact of sediment particles with the seabed surface during the flow period, this approach cannot be fully applied to describe time-dependent sediment entrainment at the ripple crest level, as sediment-laden vortices are detached from the ripple crest at the time of the flow reversal. NIELSEN (1979) explained that under wave action, when the flow is unsteady, there is no instantaneous equilibrium between the bed shear stress and the suspended sediment concentration (non-equilibrium conditions). Hence, under unsteady flow conditions, upward sediment flux at the seabed should be defined in the form of a pick-up function, $\mathrm{p(t)}$:

$$-\varepsilon_s \frac{\partial c}{\partial z} = \mathrm{p(t)} \tag{22}$$

Moreover, the sediment concentration close to the seabed increases when dense sediment clouds settle from above, while at this moment, the shear stress at the seabed is zero. It is therefore obvious that the time dependency of $\mathrm{c(z_0, t)}$ cannot be prescribed directly ($c(z_0, t)=c_0(t)$) without assuming instantaneous equilibrium between the flow condition and sediment concentration (NIELSEN, 1979, 1992). For this reason, a number of studies (VAN RIJN, 1984; THORNE et al., 2002; DAVIES and THORNE, 2005) suggest a different modelling approach based on different boundary conditions in which sediment entrainment and sediment deposition are considered independently (NIELSEN, 1992).

6.2 Pick-up function for sediment entrainment

NIELSEN (1992) explained that because an analysis of the time-dependent shear stress is very complicated, it is very difficult to derive a formula using the instantaneous Shields parameter, $\theta'(t)$. He subsequently suggested using a time-varying sediment pick-up function based on the gradient of the suspended sediment concentration near the seabed ($\partial c/\partial z$) to overcome the difficulties associated with a varying reference concentration based on the grain roughness Shields parameter (NIELSEN, 1992; SOULSBY, 1997). As mentioned in Section 5.2 (also discussed in previous studies, e.g. by HOMMA and HORIKAWA, 1962; NAKATO et al., 1977; NIELSEN, 1992; VAN DER WERF, 2006; THORNE et al., 2003; DAVIES and THORNE, 2005), the concentration event near a rippled seabed is represented by several peaks during a wave cycle, which corresponds to the action of sediment-laden vortices close to the ripple surface. This indicates that the entrainment of sand particles is closely related to the significant change in the wave bottom boundary layer and consequently to the breakdown of sand particle friction at the seabed followed by the detachment of sedimentary structures from the seabed surface and their advection into the water column above the seabed. From the point of view of sediment transport modelling of the phase-dependent suspended sediment transport near a rippled seabed induced by non-breaking waves, sediment entrainment should therefore be based on a cyclic ejection of the bed sediment particles into the water column. This pulsating ejection mechanism is described by a pick-up function, $p(t)$, which should have one input peak during each wave half-cycle at the time of flow reversal when suspended particles are entrained into the water column by the generated lee vortices. This ejection mechanism takes into account the sediment entrainment event above the observed ripple (see also Sections 5.2 and 5.2) while neglecting the "disturbing peaks" from adjacent ripples. The pick-up function, $p(t)$, is thus a non-negative function which describes the phase-dependent sediment concentrations, $c(x, 0, t)$, entrained into the water column. The spatial variation of the suspended sediment concentration can generally be described by the conservation equation:

$$\frac{\partial c}{\partial t} = -div(u_s c) \tag{23}$$

As mentioned in the last Section, there is no instantaneous equilibrium regarding the amount of picked-up sediment under unsteady flow conditions (e.g. waves). This "disequilibrium" can be prescribed using an appropriate pick-up function (NIELSEN, 1984; SVENDSEN, 1977), which requires the following boundary conditions:

$$z = 0: -\varepsilon_s \frac{\partial c}{\partial z} = p(t)$$

$$z \to \infty: c_s = 0$$

$$\text{Periodicity: } c(z, t + T) = c(z, t) \tag{24}$$

NIELSEN (1979) introduced a non-negative function with one distinct peak during each wave half-cycle, which is derived from observations of the concentration fields as follows:

$$p(t) = \frac{P_0}{1+\mu}\frac{(2m)!!}{(2m-1)!!}\left[cos^{2m}\frac{1}{2}(\omega t - \psi^+) + \mu\, cos^{2m}\frac{1}{2}(\omega t - \psi^-)\right] \quad (25)$$

where P_0 is the reference pick-up value, m the peak enhancement coefficient (a positive integer), and ψ^+ and ψ^- the phase angles of the zero down-crossing and zero up-crossing of the wave-induced flow velocity, respectively. Figure 22 a shows the variation of the normalised phase-dependent pick-up function, $p(\phi)/P_0$, with different values of the peak enhancement factor, m =2-40. It is clear that the coefficient m controls the enhancement of the concentration peaks, which in turn corresponds to the density of the near-bed sedimentary structures. This means that any increase in the enhancement factor, m, should control the increase in the entrained sediment concentration and consequently the increase in hydrodynamic forcing at the time of entrainment (i.e. at the time of the flow reversal). This offers a means of prescribing a value for m which takes account of the instantaneous hydrodynamics. Figure 22-b shows the interaction between the ratio of the extreme concentration peak to the phase-averaged mean concentration, $C^+/\langle\overline{C_0}\rangle$, and the wave steepness, H/L, above steep ripples beneath regular waves for a constant wave period, T= 5s and varying wave height (H=0.8, 1.0 and 1.2m). The panel inset shows the tendency of an increase in the concentration peak with increasing wave steepness. Although a number of representative results are required to confirm a representative trend, a first indication of the proportionality between the intensity of the near-bed suspended sediment concentration event described by the ratio $C^+/\langle\overline{C_0}\rangle$ and the hydrodynamic forcing described by the wave steepness, H/L, is established.

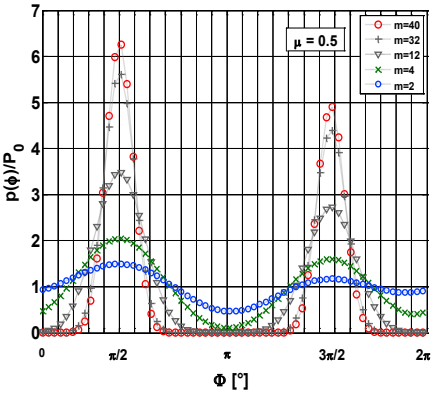

a) Effect of m on the ratio $P(\phi)/P_0$

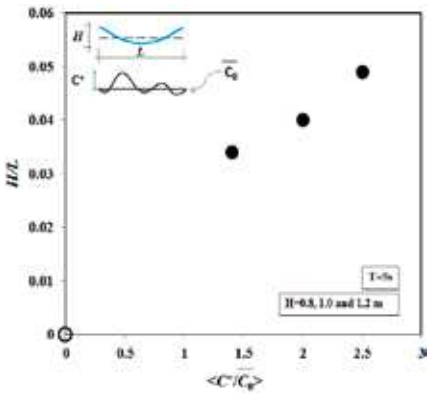

b) Effect of wave steepness on $c^+/\langle\overline{c_0}\rangle$ (see Figure 6.2)

Figure 22: (a) Variation of the ratio $P(\phi)/P_0$ with increasing peak enhancement factor, m, for a constant asymmetry shape factor, μ, and (b) Variation of the positive extreme concentration peak normalised by the phase-averaged mean concentration, $C^+/\langle\overline{C_0}\rangle$, with wave steepness, H/L

Moreover, due to the fact that the Shields parameter, θ, is proportional to the square of the velocity amplitude, the characteristics of the phase-dependent sediment entrainment above a rippled

seabed represented by the suspended sediment concentration peaks in a phase ensemble averaged concentration domain must correspond to the asymmetry shape factor, μ, as suggested by NIELSEN (1979):

$$\mu = \left(\frac{U^-}{U^+}\right)^2 \tag{26}$$

where U^- and U^+ denote the extreme velocities under wave troughs and wave crests, respectively, within a phase ensemble averaged wave cycle. Figure 23 shows a comparison between the normalised phase-dependent reference concentration with the phase ensemble averaged reference concentration, $<c_0(\phi)/\overline{C_0}(\phi)>$, and the normalised pick-up function, , $p(\phi)/P_0$, calculated using Equation (25) for the phase ensemble averaged concentration field over a large number of successive wave cycles for a) irregular waves and b) regular waves, respectively.

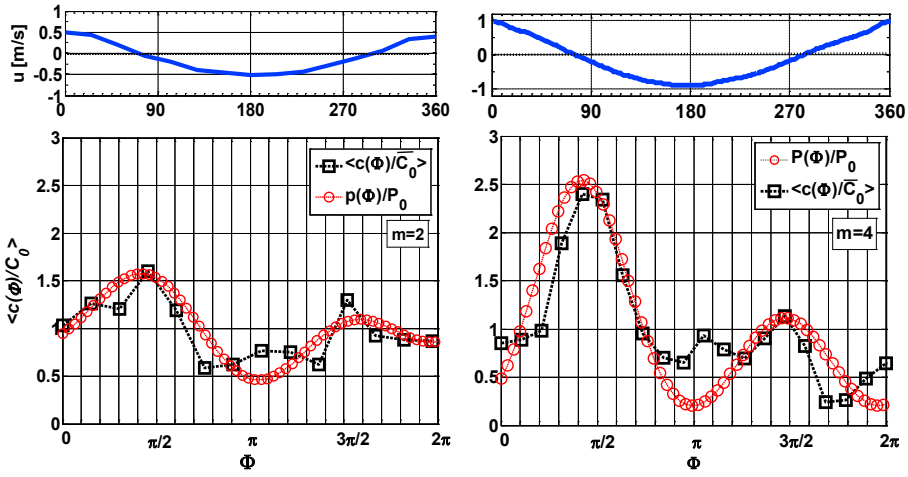

a) $C^+/\langle\overline{C_0}\rangle \approx 1.5$, μ=0.695, m=2 b) $C^+/\langle\overline{C_0}\rangle \approx 2.5$, μ=0.438, m=4

Figure 23: Comparison between the measured normalised phase ensemble averaged reference concentration, $<c_0(\phi)/\overline{C_0}>$, and that predicted by the pick-up function, $p(\phi)/P_0$, (Equation 6.4) for (a) irregular waves and (b) regular waves

As can be seen in Figure 23, the extreme concentration peaks representing suspended sediment ejections at the times of flow reversal (at $\phi \approx \pi/2$ and $3\pi/2$) are reasonably well predicted by the pick-up function (Equation 25) using (a) a peak enhancement factor of m=2 and 4 by $C^+/\langle\overline{C_0}\rangle$ =1.5 and (b) a peak enhancement factor of m=4 with $C^+/\langle\overline{C_0}\rangle$ = 2.5 (see also Figure 6.1). As illustrated by Figure 22 b, the ratios $C^+/\langle\overline{C_0}\rangle$ =1.5 and 2.5, corresponding to H/L=0.034 and 0.048, respectively, can be reasonably represented using m=2 and 4 in the pick-up function, $p(t)$, (Equation 25). Additionally, the proportionality between the negative and positive extreme concentration peaks, C^- and , C^+ which occur during the negative and positive wave half-cycles under the maximum negative and maximum positive wave-induced flow velocities, U^- and U^+, can be well estimated using the asymmetry factors $\mu = (U^-/U^+)^2$ = 0.695 and 0.438, respectively (see Equation 25; cf. Figure 23 a and b).

6.3 1DV model for predicting wave-induced suspended sediment transport

According to NIELSEN (1992), if the mixing length, l_m, is small compared to the overall height of the vertical concentration profile, the mixing process is essentially diffusive and the pure gradient diffusion solution can be used to describe the upward sediment flux. Conversely, if the mixing length, l_m, is of the same order of magnitude of the overall height of the concentration profile, the mixing process is convective and a different modelling concept must be applied. In this context, THORNE et al. (2002) suggested that for the first near-bed layer ($z<3\eta_r$), a pure gradient diffusion solution characterised by a near-bed sediment diffusivity represents an appropriate modelling strategy, whereas for the area above this layer, the convection-diffusion solution might be more applicable. Against this background, a predictive 1DV mathematical semi-analytical modelling concept is now considered for modelling the time-dependent suspended sediment entrainment above the seabed under the action of non-breaking regular and irregular waves. This modelling concept is based on the continuity equation above a horizontally-averaged seabed level. The model was parameterised using the hydrodynamic and morphodynamic measurements obtained from the large-scale tests performed in this study for both non-breaking regular and irregular wave regimes (see Sections 3, 4, 5). As extensively discussed in Section 5, within a layer with a thickness of about $3\eta_r$ above a rippled seabed (η_r is the ripple height) (layers a and b in Figure 6.12, Section 6.1.6 in AHMARI, 2012), the wave bottom boundary layer separates on the leeward side of the ripple. Vortices are thus generated on the leeward side of the ripples due to momentum transfer. Above this layer, $z>3\eta_r$, the shedding of sediment-rich detached vortices occurs at the time of flow reversal (layer c in Figure 6.12, Section 6.1.6 in AHMARI, 2012). Furthermore, observations indicate that at higher elevations, the coherent sediment-laden structures almost disappear and sediment clouds are transported by random turbulence (THORNE et al., 2002). This confirms the fact that the transport of suspended particles under wave-induced flow at higher elevations become more uniform compared to that close to the seabed ($0<z<3\eta_r$). This demonstrates the importance of the concentration event close to the ripple surface compared to the concentration event in upper layers.

6.4 Governing equations

The 1DV model proposed by NIELSEN (1979) for the time-dependent phase ensemble averaged intrawave suspended sediment transport above a rippled seabed during a wave cycle is extensively described in the following. For the 1DV modelling of time-dependent sediment entrainment, the following two basic assumptions are necessary (SVENDSEN, 1977; NIELSEN, 1979):

- All sediment particles move in suspension, as represented by the dominance of suspended load in a non-breaking wave regime above ripples.
- The sediment fraction that settles at the level of the ripple crest, $w_s \, . \, c(0,t)$, and the sediment fraction picked up, $p(t) = -\varepsilon_s(\partial c/\partial z)$, are treated separately.

The governing equation that describes the temporal distribution of the suspended sediment concentration, $\partial c/\partial t$, is the conservation equation. This may be approximated by the one-dimensional non-steady diffusion equation as follows:

$$\frac{\partial c}{\partial t} - w_s \frac{\partial c}{\partial z} - \frac{\partial}{\partial z}\left(\varepsilon_s \frac{\partial c}{\partial z}\right) = 0 \tag{27}$$

where ε_s is the sediment diffusivity and w_s the settling velocity. In order to model the periodic nature of wave-induced sediment entrainment around sand ripples, the corresponding functions are considered in terms of their Fourier components. According to NIELSEN (1979), complex formulations are used to simplify all calculations, considering the fact that the physical properties correspond to the real part of the complex numbers:

$$c_n(z,t) = \sum_0^N c_n \, e^{in\omega t} \, \zeta_n \tag{28}$$

where $c_n \, e^{in\omega t}$ is the periodic component of $c_n(z,t)$ with a period T/n. According to NIELSEN (1979), in the case of rippled seabeds under the action of non-breaking waves, where the sediment diffusivity remains constant in a near-bed layer with a thickness of $z \approx 3\eta_r$ (see Section 6.1.6, Figure 6.12 in AHMARI, 2012), an ordinary linear differential equation can be written as follows by inserting Equation (28) into Equation (27) and dividing by $c_n \, e^{in\omega t}$:

$$\zeta''_n + \left(\frac{w_s}{\varepsilon_s}\right) \zeta'_n - i\frac{n\omega}{\varepsilon_s} \, \zeta_n = 0 \tag{29}$$

where " ´ " denotes a differentiation with respect to z and ζ_n:

$$\zeta_n = e^{-\frac{w_s}{\varepsilon_s}\alpha_n} \tag{30}$$

where:

$$\alpha_n = \frac{1}{2} + \sqrt{\frac{1}{4} + i\frac{n\omega\varepsilon_s}{{w_s}^2}} \tag{31}$$

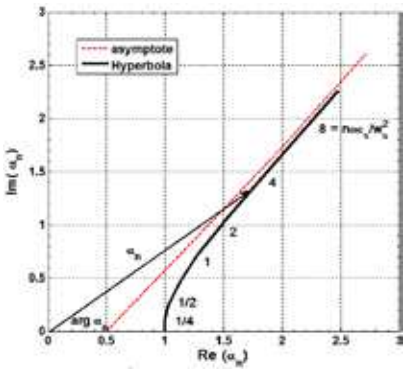

Figure 24: Variation of the complex number α_n for the pure diffusive solution (Equation 6.10 in NIELSEN, 1992)

Figure 24 shows the variation of the complex coefficient, α_n. NIELSEN (1992) underlined the fact that in case of the pure diffusive solution the coefficient α_n differs from the complex coefficient for pure convection, β_n, since the real part of parameter α_n, $\mathrm{Re}\{\alpha_n\}$, is a function of the radian frequency, ω, and the imaginary part of α_n, $\mathrm{Im}\{\alpha_n\}$, is not proportional to $n\omega$. This means that the different harmonic components of the diffusion formulation decay at different rates with elevation, z, and their time lags grow at different rates with z. Further, Figure 24 shows that the individual Fourier components, $c_n(z,t)$, decay with radian frequency (for more details, see NIELSEN, 1992). Moreover, the phase lag of the Fourier components grow differently with z, which is crucial regarding the observed increasing phase lags between the pick-up function at the ripple and the shedding process at higher elevations and represents the rapid blurring of the concentration peaks above steep ripples discussed in Section 6. Considering the boundary conditions given in Equation (24) and a simple harmonic pick-up function of the following form:

$$p(t) = P_n e^{in\omega t} \tag{32}$$

where P_n is the amplitude of the n-th harmonic of $p(t)$:

$$P_n = \frac{P_0 . a_n}{1+\mu}, \; P_0 = C_0 w \tag{33}$$

μ is the asymmetry shape factor, and:

$$\begin{cases} a_1 = \frac{2m}{(m+1)}, & n = 1 \\ a_n = \frac{2m}{(m+1)} \; \dots \; \frac{m-(n-1)}{(m+n)} \dots, & n = 2,3,4,\dots \end{cases} \tag{34}$$

Where m is the peak enhancement coefficient.

By inserting Equations (30) and (31) into Equation (28) and taking into account the complex coefficient $(P_n/w\alpha_n)e^{-in\omega t}$ based on the boundary conditions (Equations 22 and 32), Equation (28) is inferred for modelling the distribution of suspended sediment concentration in both time and space above rippled seabeds beneath non-breaking waves as follows:

$$c(z,t) = \sum_0^N \frac{P_n}{w_s\left(\frac{1}{2}+\sqrt{\frac{1}{4}+i\frac{n\omega\varepsilon_s}{{w_s}^2}}\right)} e^{in\omega t} e^{-\frac{w_s z}{\varepsilon_s}\left(\frac{1}{2}+\sqrt{\frac{1}{4}+i\frac{n\omega\varepsilon_s}{{w_s}^2}}\right)} \tag{35}$$

Due to the fact that the physical phenomenon (here suspended sediment concentration) is expressed by taking the real part of the complex function, Equation (35) may be written as:

$$c(z,t) = \sum_0^N \frac{P_n}{w_s|\alpha_n|} e^{-\frac{w_s z}{\varepsilon_s} Re\{\alpha_n\}} \cos n[\omega t - \psi_n - \frac{1}{n}(arg\ \alpha_n + \frac{wz}{\varepsilon_s}\ Im\{\alpha_n\})] \tag{36}$$

6.5 Discussion of the considered 1DV model

As mentioned in Section 6.3, the 1DV model (Equation 36) is based on the diffusion equation and prescribes that all sediment particles are entrained in suspension. This is an important assumption for determining the phase lag between $p_n(t)$ and $c_n(z,t)$, which is clearly evident in the measured data. Equation (35) generally takes the same form as the modelling of the time-averaged vertical profile of the suspended sediment concentration distribution over the entire water column (reference concentration, c_0, times the decay term, e^{-z/l_m}), which describes the concentration distribution with height above the seabed, z. In order to describe the temporal and spatial suspended sediment concentration distribution above ripples, however, the decay of sediment concentration above the seabed should be modelled more precisely. As indicated by Equation (35), the total phase lag of the suspended sediment concentration decay with height above the seabed can be modelled in both time (second term) and space (third term) separately. This separation of the phase lag between sediment entrainment and $c(z,t)$ is especially appropriate above steep ripples, where the generation of vortices on the leeward side of ripples and the shedding process during flow reversal depend on the concentration decay length above the ripple crest ($l_m = \varepsilon_s/w_s$) as well as the times of flow reversal ($\omega t\text{-}\psi^{\pm}$). This can clearly be seen by examining the intrawave phase ensemble averaged concentration patterns presented in Section 5 (see Figures 13 and 14). Due to the fact that the coefficient α_n is a function of $n\omega$ and $\mathrm{Re}\{\alpha_n\}>1$, the different harmonic components of $c_n(z,t)$ decay differently with z. This is crucial regarding the limitation of the high suspended sediment concentration event close to the seabed, which tails off rapidly with height above the seabed such that the suspended sediment movement becomes fairly uniform when $z > 3\eta_r$ (see Section 6.1.6 in AHMARI, 2012). Furthermore, since the imaginary part of α_n, $\mathrm{Im}\{\alpha_n\}$, is not proportional to $n\omega$ and $\mathrm{Im}\{\alpha_n\}>0$, the phase lag between sediment pick-up on the seabed and the sediment suspension transported at higher levels increases with z. In the formulation based on pure convection, on the other hand, the harmonic components and the time lag between $c(0,t)$ and $\int_0^\infty c(z,t)dz$ decay at the same rate at each elevation, z. This is due to the fact that in the pure convection solution, the real part of β_n is $\mathrm{Re}\{\beta_n\}=1$ for all ω and the imaginary part $\mathrm{Im}\{\beta_n\}$ is a function of ω. Furthermore, the time lag grows at the same rate with z for all frequencies (for details of the pure convection solution, see NIELSEN, 1992). Moreover, the vertical decay length scale of the suspended sediment concentration, l_m, is replaced here by ε_s/w_s (NIELSEN, 1979). With regard to the sediment diffusivity, ε_s, Equations (17) and (36) are used to account for the constant sediment diffusivity induced by regular and irregular waves, respectively, close to a rippled seabed ($z < 1.5k_s$). This is calculated from the vertical profiles of the time-averaged ABS concentrations measured during the tests performed in the Group 1 experiments (see Table 3). As indicated by observations of the small-scale intrawave sediment entrainment above ripples for non-breaking regular and irregular waves, the weak asymmetry of the Stokes waves results in slight differences in the concentration fields between two wave half-cycles. For instance, Figure 14 shows that beneath weakly-asymmetric non-breaking Stokes waves, the concentration events in the first wave half-cycle under positively directed wave-induced near-bed flow are clearly larger than during the second wave half-cycle. This is due to the lower negative flow velocity amplitude close to the seabed compared to the higher positive flow velocity amplitude during the first wave half-cycle. Due to the fact that the amount of entrained sediment is almost proportional to the Shields parameter, θ, which is in turn proportional to the square of the velocity amplitude, NIELSEN (1979) suggest-

ed using the asymmetry coefficient, μ, to take account of this effect (Equation 26). Accordingly, Equation (36) may be reformulated:

$$c(z,t) = \sum_0^N \frac{P_n}{w_s\,|\alpha_n|}\,[cos\ n\left(\omega t - \psi^+ - \frac{1}{n}(arg\ \alpha_n + \frac{w_s z}{\varepsilon_s}\ Im\{\alpha_n\})\right)$$

$$+\mu\ cos\, n\left(\omega t - \psi^- - \frac{1}{n}(arg\ \alpha_n + \frac{w_s z}{\varepsilon_s}\ I_m\{\alpha_n\})\right)]\ e^{-\frac{w_s z}{\varepsilon_s} Re\,\{\alpha_n\}} \qquad (37)$$

Moreover, as mentioned in Section 6.2, the proportionality between wave steepness, H/L, and the positive extreme concentration peak normalised with the phase ensemble averaged mean concentration ($C^+/\langle\overline{C_0}\rangle$) may be applied to control the positive integer, m, which is tentatively illustrated in Figure 22. Another important implication of the observations of small-scale intra-wave sediment entrainment processes above a rippled seabed beneath non-breaking waves discussed in Section 5 is the period of entrainment of the sediment-laden vortices that detach from the ripple crests during flow reversal. As mentioned in Section 5 (see also AHMARI, 2012; Section 6), the almost fully-laden lee vortices which are detached on the steep ripple crests eject sediment particles into the water column twice during each wave cycle. The time period of vortex detachment is calculated from simultaneous measurements of the temporal distribution of suspended sediment concentration and the wave-induced near-bed flow velocity, which is represented in the concentration formula by the periods of release of lee vortices (ψ_n^+ and ψ_n^-). Furthermore, the effects of ripple steepness, $C^+/\langle\overline{C_0}\rangle$, and the mean sediment grain size, d_{50}, are taken into account in Equation (37) by means of the concentration decay length ($l_m = \varepsilon_s/w_s$; see Equation (17) for ε_s and Equation (11) for w_s).

6.6 Comparison of computed results and ABS measurements

In order to demonstrate the accuracy of the time-dependent sediment concentration distribution predictions for non-breaking regular and irregular waves using the 1DV transport model presented in AHMARI (2012), the computed values were compared with the phase ensemble averaged suspended sediment concentrations determined from the ABS measurements. Two examples were chosen for this purpose, which correspond to irregular and regular wave sequences. An extensive analysis of the phase ensemble and bed-averaged intrawave sediment concentration entrainment patterns for these two examples were extensively discussed in Section 5.3 of presented paper (regular wave condition) and in Section 6.4.2 in AHMARI 2012 (irregular wave condition). The input parameters of the presented 1DV model for irregular and regular waves are listed in Table 9.

Table 9: 1DV model input parameters for irregular and regular waves

Parameter	Irregular waves (H_s= 1m, T_p= 5 s) (Figure -a)	Regular waves (H= 1.2 m, T= 5 s) (Figure -b)
Wave steepness, H/L [-]	0.044	0.057
Relative wave height, h/H [-]	2.87	2.20
Wave asymmetry, U^-/U^+ [-]	0.774	0.658
Peak enhancement factor, m [-]	2	4
Near bed velocity amplitude, $U=A\omega$ [m/s]	0.68	0.93
Settling velocity, w_s [m/s]	0.028	0.028
Ripple steepness, η_r/λ_r [-]	0.15	0.14
Equivalent bed roughness, $k_s = 25\,\eta_r(\eta_r/\lambda_r)$ [m]	0.19	0.175
Sediment diffusivity, $\varepsilon_s = 0.0112 U k_s$ [m²/s]	0.00144	0.00182

Figures 25 ii and 25 iii show the measured and predicted contour plots of the phase ensemble averaged intrawave concentration fields above ripples in 2 tests performed for irregular and regular wave sequences. The results are shown from 1cm above the ripple crest level up to a relative height of z/η_r=3 above the seabed (≈ 15 cm above the ripple crest level), together with the wave-induced flow velocity measured by an ECM at 25 cm above the initial seabed level (Figure 25 i-a and b). As can be seen in Figure 25 ii-a and b, the main peaks of entrained concentrations for both irregular and regular wave regimes occur around the time of first flow reversal following the passage of the wave crest at $\omega t \approx 90°$. These then decay with height and suffer a phase lag which increases with height above the seabed. The secondary less-pronounced concentration peaks occur just before the time of second flow reversal following the extreme negative wave-induced flow velocity at $\omega t \approx 270°$ and are also subject to the same attenuation and phase lag with increasing height above the seabed. The calculated results shown in Figure 25 iii for irregular and regular wave regimes (panels a and b, respectively) show similar SSC features as the observed concentration fields shown in Figure 25 ii. As can be seen in Figure 25, the times of the two observed concentration peaks at the points of flow reversal as well as the changes in their attenuations and phase lags with height above the seabed are correctly reproduced. Moreover, good agreement is obtained between the measured asymmetry in the ABS concentration patterns due to the different magnitudes of the concentration peaks during the positive and negative wave half-cycles and the values predicted by the 1DV model. Furthermore, a comparison between the predicted and measured values of the suspended sediment entrainment event close to the seabed illustrated in Figure 25 shows that a high proportion of the time-dependent suspended sediment concentration event occurs in a layer just above the ripple crest height with the thickness of about 3 times the ripple height ($3\eta_r \approx$ 15 cm for focused ripples). This includes (i) the generation of sediment-laden vortices on the leeward sides of the ripples, (ii) the ejection of detached

sediment-rich vortices into the water column, (iii) the shedding process after reversal of the wave-induced near-bed flow direction and (iv) the onset of disintegration of coherent sedimentary structures. Above this height, the movement of the sediment clouds is more or less uniform and the time-dependency of the suspended sediment concentration decreases drastically. This behaviour is in good agreement with the governing processes at a height of $3\eta_r$ above the seabed, where the sediment diffusivity remains constant due to the effect of the ripples and the dominance of the coherent sedimentary structures, as extensively discussed in AHMARI (2012).

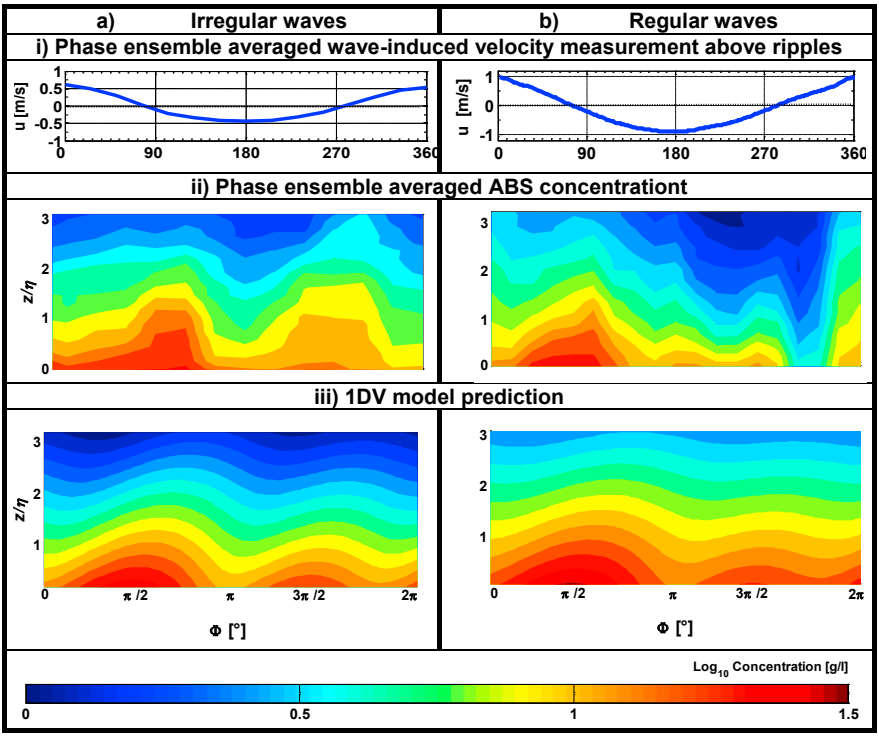

Figure 25: Comparison between measured phase ensemble and ripple-averaged intrawave concentration fields around ripples and the values predicted by the 1DV model based on the diffusion equation for a) irregular waves (H_s= 1.0m, T_p=5s, h≈ 3.2m) and b) and b) regular waves (H=1.2m, T=5s h≈3.18m)

Moreover, Figure 26 shows the predicted and measured vertical profiles of the time-averaged and bed-averaged suspended sediment distribution above the ripple crest for both irregular and regular waves, as illustrated in panels a and b, respectively. As can be seen in Figure 26, the decay gradient of the suspended sediment concentration is relatively well predicted by the 1DV model. However, the predicted time-averaged and ripple-averaged suspended sediment concentrations are somewhat underestimated for irregular waves (≈10%) and somewhat overestimated for regular waves (≈13%). This is due to the nature of the pick-up function with more pronounced concentration peaks near the times of flow reversal for regular waves, resulting in larger suspended sediment concentrations at greater heights above the seabed. A comparison between Figure 26 a and 26 b indicates that at low concentration levels, the difference between the measured and predicted concentration profiles decreases.

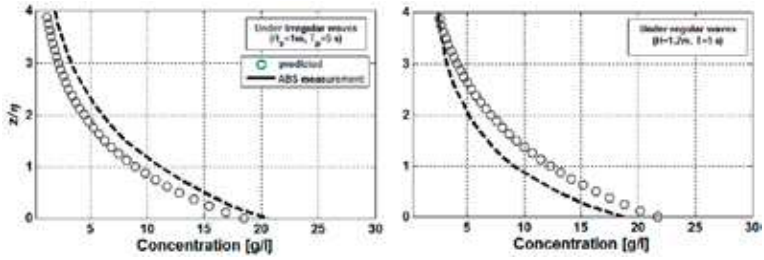

a) H_s= 1m, T_p=5s, h=3.2m b) H= 1.2m, T=5s, h=3.2m

Figure 26: Predicted and measured vertical profiles of the time-averaged suspended sediment concentration above ripple crests for a) irregular waves b) regular waves

7. Concluding remarks and recommendations for further research

Most of our present knowledge relating to wave-induced sediment transport is based on laboratory experiments. However, the data sets from previous measurements, particularly above rippled seabeds, are partly incomplete and cannot provide a full picture of the intrawave entrainment processes of suspended sand particles for a diversity of near-bed hydrodynamic regimes. Furthermore, no model appears to exist so far that can reliably reproduce such a full picture. The new full-scale measurements of near-bed wave-induced flow and sediment concentration performed in the Large Wave Flume (GWK) over a complete beach profile for different groups of regular and irregular waves have demonstrated the importance of precise measurements of time-dependent suspended sediment concentration above both plane and rippled seabeds. An extensive comparative analysis of the data sets obtained using optical, acoustic and mechanical measuring devices revealed that the multi-frequency Acoustic Backscattering System (ABS) is clearly the most suitable device for measuring sediment entrainment over steep ripples at different seabed locations simultaneously with sufficient temporal and spatial accuracy.

An intrawave analysis of the ABS data set demonstrates that the preliminary entrainment of sand particles in a rippled bed regime, as observed as sediment concentration peaks within a wave cycle, occurs in a crucial near-bed layer with a thickness of $z \approx 3\eta_r$. In this layer of high coherent sedimentary structures with increased equivalent bed roughness due to steep ripples ($k_s \approx 2.6\,\eta_r$ for irregular waves and $k_s \approx 3\eta_r$ for regular waves), the sediment diffusivity remains constant with height above the seabed. Above this layer ($z > 3\eta_r$), the coherent vortex structures break up and the sediment diffusivity attains a maximum value. At higher elevations, the magnitude of suspended sediment concentration decreases rapidly, the coherent structures completely disintegrate, and the effect of random turbulence on sediment transport becomes considerable.

In contrast to the transport processes above rippled seabeds beneath near-breaking waves (high near-bed flow energy), coherent structures do not form above plane seabeds due to the absence of steep ripples and sediment particles are transported within a very thin sheet-flow layer (z/d_{50} <15). Above this thin sheet-flow layer, low sediment ejection into the water column is observed, which is negligible compared to the number of sediment particles transported in the sheet-flow layer.

A comparative analysis of predicted and measured sediment diffusivity above low ripples beneath non-breaking waves (previous studies) and above a plane seabed beneath near-breaking waves (present study) show that k_s =2.5 d_{50} represents the equivalent bed roughness more reliably than $k_s = 25\eta_r(\eta_r/\lambda_r)$ above a seabed covered with very low ripples, which reacts dynamically as a plane seabed. Moreover, the predicted sediment diffusivity above a plane seabed in a high near-bed flow energy regime using the formulation of VAN RIJN (1993) was found to agree well with the value of k_s =2.5 d_{50} based on the measurements performed in the present study.

In the case of rippled seabeds, the bed load is transported in the onshore direction, whereas the net suspended sediment flux is in the offshore direction. The former is due to the onshore-directed ripple migration induced by asymmetric waves while the latter is due to subsequent vortex formation on the leeward sides of ripples and the phase lags associated with reversed wave-induced near-bed flow. In contrast to this, the net sediment flux in a near-breaking wave regime is directed onshore above a plane seabed and occurs in a very thin sheet-flow layer.

The intrawave analysis of sediment concentration beneath irregular waves confirmed that the variation of the non-dimensional ratio d_0/λ_r is more pronounced than in the case of regular waves. A lower limit of 1.2 can thus be specified for the ratio d_0/λ_r, above which the shedding of generated lee-vortices is expected to occur around the time of flow reversal, and below which vortex shedding is not expected.

Moreover, the analysis of the experimental results highlights the importance of the effect of non-breaking and near-breaking waves on sediment entrainment above both rippled and plane seabeds, thereby permitting a quantification of the governing processes in the nearshore zone.

Due to the dominance of a rough turbulent flow regime in the wave-breaking zone, a considerable amount of air is entrained into the water column, which increases the turbulence intensity for pronounced wave-breaking events (plunging breakers). The entrained air bubbles roll together with the broken waves towards the swash zone. This high air bubble entrainment results in high interception of the ABS signal and partial loss of the bed echo.

Moreover, due to the fact that an air bubble also represents a target for the acoustic backscattering inversion just as the suspended sand particle itself, this means that it is hardly possible to distinguish an air bubble from a suspended sand particle. Considering the fact that a large amount of air entrained by rolling breakers is always present in the upper water column of the surf zone, the sediment concentrations determined from backscatter inversion in the inner surf zone will consistently be underestimated.

An exponential decrease in the suspended sediment concentration with height above the sea bed based on a reference concentration was taken as a basis for predicting the time-averaged vertical distribution of suspended sediment concentration. This is the most well-established method for modelling the suspended sand distribution above the seabed, using a mixing decay length, l_m, , and a reference concentration C_0. Good agreement with the reference concentration measured in the GWK was obtained using the exponential form of decreasing suspended sediment concentration. However, the concentration decay length l_m=1.4η_r suggested by NIELSEN (1986) was modified in the present study to yield a value of l_m=2η_r for U_0/w_s>18.

Moreover, the large-scale experiments generally confirmed the expression suggested by NIELSEN (1986) to calculate the reference concentration C_0. However, a new reference concentration formula is proposed in this study using the empirical coefficient, $\alpha = 0.00385 \pm 0.00115$, which lies some-

where between $\alpha = 0.0022 + 0.0005$ introduced by NIELSEN (1986) and the modified value of $\alpha = 0.0022 + 0{\cdot}0005$ given by THORNE et al. (2002).

A one-dimensional vertical modelling concept proposed by NIELSEN (1979) was applied to predict the time-dependent distribution of suspended sediment concentration above ripples based on the pure diffusion equation. This model was parameterised using the data set determined from measurements in the present study. A comparison between the predicted values and the values measured by the ABS demonstrates the ability of the model to correctly predict concentration peaks as well as the temporal and spatial phase lags between lee vortex formation and transportation of the suspended sediment concentration.

The range of application of the proposed 1DV model is restricted to areas with relatively low mobility number ($\psi < 110$; non-breaking wave regime; low near-bed flow energy) where the seabed is covered with steep ripples and wave-induced suspended load represents the dominant sediment transport mode.

A comparison of the phase ensemble averaged concentration patterns within a wave half-cycle show that the concentration values predicted by the 1DV are slightly overestimated (≈13%) for regular waves and slightly underestimated (≈10%) for irregular waves. This effect was found to be more pronounced in both cases at higher concentration levels.

The ABS concentration measurements in the GWK for a very tough flow regime induced by breaking and broken waves (Test Group 4 shown in Figure 2; Table 4) were unable to contribute to a better understanding and quantification of sediment transport processes under such conditions due to the instability of the acoustic signals in the presence of entrained air bubbles. New experiments should hence be performed under similar conditions to those in the present study with the additional implementation of a consistent strategy to simultaneously measure the quantity of entrained air bubbles. This may contribute to a better understanding of the effect of air entrainment on the suspension processes and possibly also help filter out the disturbing air bubble effect from the measured suspended sediment concentration data. Moreover, a comparison between the measured and predicted ripple size (cf. Section 6.1 in present paper and Section 5.2.1 in AHMARI, 2012) demonstrates that more precise investigations of non-equilibrium ripples (generation, steepening, flattening, migration) are required to verify and possibly improve the reliability of existing empirical formulae for predicting ripple geometry. Furthermore, the mathematical model presented in this study predicts the suspended sand transport processes in a purely wave-induced oscillatory flow regime over rippled seabeds in which all of the sand particles move as suspended load. Under field conditions, however, sand particles are also transported above diverse seabed forms, which range from rippled to plane seabeds under the combined action of both waves and currents. Finally, five further possible improvements are suggested in the following to help improve the prediction of sediment transport as well as to develop more suitable models for engineering practice:

- Consideration of the higher mobility induced under storm conditions (near-breaking asymmetrical waves; ripple wash-out situation) in order to predict sediment transport in the sheet-flow mode resulting from large onshore-directed wave-induced flow velocities, including validation of the new sheet-flow sub-model using the data sets obtained in this study.
- Prediction of sediment entrainment and distribution under the action of breaking and broken waves in a tough turbulent flow regime (very high mobility; combination of a plane and rippled seabed), taking into account the effects of turbulent eddies and entrained air bubbles in the inner surf zone due to plunging wave breakers. The first step to achieve this goal would

be to analyse the data sets in the inner surf zone determined from the full-scale ABS concentration measurements in this study (Test Group 4, see Figure 3.1) after possible filtering of the air bubble effect.

- Prediction of sediment pick-up induced by irregular waves above rippled and plane seabeds using a shear stress concept (e.g. $p(t) = f(\theta'(t))$; where $p(t)$ is a time-dependent pick-up function and $\theta'(t)$ is a phase-dependent effective Shields parameter).
- Extension of the 1-DV pure gradient diffusion model to a 2-DV diffusion-convection model and consideration of the bed load and suspension load above rippled seabeds together by taking into account the convective terms of the convection-diffusion equation.
- Prediction of sediment flux under the combined action of waves and currents. For this purpose, a shear stress concept could also be applied to model the effects of the net current on sediment entrainment. In order to validate the predictions given by such a model, however, new full-scale experiments would be necessary in large-scale facilities which permit the simulation and superimposition of oscillatory flows and currents (e.g. oscillating water tunnels).

8. Acknowledgements

A number of experiments presented in this paper was partly supported by the BMBF within the scope of the Project "ModPro" (03KIS060). However, most of the experiments were conducted in many phases over several years and were fully-supported by the European Community within the Sixth Framework Programme as part of the Joint Research Activity "SANDS" within the framework of the Integrated Infrastructure Initiative HYDRALAB III . The support given by Mr. J. Grüne and the GWK team in performing the experiments of both projects as well as the valuable assistance of Prof. Kos'yan during the ModPro-Project are gratefully acknowledged. The author also expresses his thanks to Dr. Ian Westwood for his meticulous proofreading of the final manuscript.

9. References

AHMARI, A.: Suspended sediment transport above a rippled and plane seabed induced by non-breaking and near-breaking waves. A large-scale laboratory study. Ph.D. thesis, Technical University of Brunswick, Germany, 2012.

ANDERSEN, K. H.: Ripples beneath surface waves and topics in shell models of turbulence. Ph.D. thesis, University of Copenhagen, Denmark, 1999.

BOSMAN, J. J.: Concentration measurements under oscillatory motion. Technical Report M1695 Part II, Delft Hydraulics, The Netherlands, 1982.

BOSMAN, J. J. and STEETZEL, H. J.: Time- and bed-averaged concentration under waves. Rep. 385, Delft Hydraulics, The Netherlands, 1988.

BOSMAN, J. J; VAN DER VELDEN, E. T. J. M. and HULSBERGEN, C. H: Sediment Concentration Measurement by Transverse Suction. In: J. of Coastal Engineering, Vol. 11, 353–370, 1987.

CLUBB, G. S.: Experimental study of vortex ripples in full-scale sinusoidal and asymmetric flows. PhD thesis, University of Aberdeen, UK, 2001.

CRICKMORE, B. A. and AKED, R. F.: Pump samplers for measuring sand transport in tidal waters. In: Proc. Conf. Instrumentation in Oceanography, Univ. Coll. North Wales, Bangor, 311-326, 1975.

DAVIES, A. G. and THORNE, P. D.: Modeling and measurement of sediment transport by waves in the vortex ripple regime. In: J. of Geophysical Research, 99(C1), C05017, 1-25, 2005.

DAVIES, A. G. and THORNE, P. D.: Advances in the study of moving sediments and evolving seabeds. In: Surveys in Geophysics, Vol. 29, 1–36, 2008.

DOUCETTE, J. S. and O'DONOGHUE, T.: Sand ripples in irregular and changing wave conditions: a review of laboratory and field studies. University of Aberdeen, Department of Engineering. EC MAST Project No. MAS3-CT97-0086, 2002.

FREDSOE, J.; ANDERSEN, O. H. and SILBERG, S.: Distribution of suspended sediment in large waves. In: ASCE , J. of Waterway, Port, Coastal and Ocean Engineering, Vol. 111, No. 6, 1041-1059, 1985.

GARCIA, H. M.: Sedimentary Engineering; Processes, Measurements, Modeling and Practice. ASCE manuals and reports on engineering practice No. 110. Published by American Society of Civil Engineering, 2007.

GRANT, W. D. and MADSEN, O. S.: Movable bed roughness in unsteady oscillatory flow. In: J. of Geophysical Research, Vol 87, No.C1, 469–481, 1982.

GRASMEIJER, B.T.; DOLPHIN, T.; VINCENT, C. E. and KLEINHANS, M. G.: Suspended sand concentrations and transports in tidal flow with and without waves. Paper U in Sandpit book ISBN90-800356-7-x, edited by Van Rijn et al. Aqua Publications, The Netherlands, 2005.

GREEN, M. O; VINCENT, C. E.; MCCAVE, I. N and DICKSON, R.R: Storm sediment transport: observations from the British north sea shelf. In: Continental Shelf Research, Vol. 15, 889–912, 1995.

GREEN, M.O. and VINCENT, C. E.: Field measurements of time-averaged suspended sediment profiles in a combined wave and current flow. Soulsby, R. and Bettess, E. (Editors). In: Sand Transport in Rivers, Estuaries and the Sea. A.A. Balkeema, Rotterdam, 25-30, 1991.

GRUENE, J.; KOS'YAN, R.; OUMERACI, H.; PODYMOV, I.; SCHMIDT-KOPPENHAGEN, R. and VINCENT, C. E.: Large-scale laboratory modelling of sand concentration fluctuations under irregular waves. In: ASCE, Proc. Coastal sediment '07, 1–11, 2007.

HANES, D.; ALYMOV, V. and CHANG, Y.: Wave-formed ripples at Duck, North Carolina. In: J. of Geophysical Research, Vol. 106 (C10), 22575–22592, 2001.

HAY, A. E.: On the remote acoustic detection of suspended sediment at long wavelengths. In: J. of Geophysical Research, Vol. 106 (C10), 7525–7542, 1983.

HOM-MA, M. and K. HORIKAWA: Suspended sediment due to wave action. In: Proc. 8th Coastal Engineering Conf, 168–193, 1962.

HUYN THANH, S.; TRAN THU, T. and TEMPERVILLE, A.: A numerical model for suspended sediment in combined currents and waves. In: Sediment transport mechanisms in coastal environments and rivers. In: Euromech 310, Le Havre, edit by M. Belorgey et al., World Sci., Singapore, 122- 130, 1994.

THORNTON, E. B.; HUCK, M. P. and STANTON, T. P.: Vertical and horizontal coherence length scales of suspended sediments. In: ASCE, Proc. Coastal Sediments'99, Vol 1-3, 225–240, 1999.

JETTE, C. D. and HANES, D. M.: Measurements of Wave Generated Bedforms. In: ASCE, Proceedings of the International Conference on Coastal Engineering (ICCE), 3129-3142, 1996.

KOS'YAN, R.; DIVINSKY, B.; GRÜNE, J.; PODYMOV, I.; VINCENT, C. E.; AHMARI, A. and OUMERACI, H.: Laboratory research of the dependence of suspended sand concentration on the spectra form of irregular waves. In: Environment Ninth Int. Conf. on the Mediterranean Coastal (Medcoast '09), Sochi, Russia, 2009a.

KOS'YAN, R. D; DIVINSKIY, B. V; KRYLENKO, M. V and VINCENT, C. E.: Modeling of the vertical distribution of suspended sediment concentration under waves with a group structure. IEEE. Oceans Conference, Aberdeen, Scotland, 1–6, 2009b.

KOS'YAN, R. D; DIVINSKIY, B. V; KRYLENKO, M. V and VINCENT, C. E.: Modeling of the vertical distribution of suspended sediment concentration under waves with a group structure. IEEE. Oceans Conference, Aberdeen, Scotland, 1–6, 2007.

KOS'YAN, R. D.; KUNZ, H.; KUZNETSOV, S.; PYKHOV, N.; PODYMOV, I. and VOROBYEV, P.: Physical regularities of suspended sand concentration and transport under irregular waves based on field data. Die Küste 64, 161–200, 2001.

KOS'YAN, R. D.; KUZNETSOV, S. Yu.; PODYMOV, I. S.; PYKHOV, N. V.; PUSHKAREV, O. V.; GRISHIN, N. N. and HARIZOMENOV, D. A.: Optical instrument for measuring of suspended sediment concentration during storm in the coastal zone. In: Okeanologiya (Oceanology), Vol. 35. № 3, 463-469, 1995.

LEE, G. H.; FRIEDRICHS, C. T. and VINCENT, C. E.: Examination of diffusion versus advection dominated sediment suspension on the inner shelf under storm and swell conditions, Duck, North Carolina. In: J. of Geophysical Research, Vol. 107(C7), 3084, 21-1-21-13, 2002.

LEE, G.; DADE, W. B.; FRIEDRICHS, C. T. and VINCENT, C. E.: Examination of reference concentration under waves. In: J. of Geophysical Research, Vol. 109, C02021, 1-10, 2004.

MARGVELASHVILI, N.: Model for estuarine and coastal sediment transport. MECOSED Scientific Manual. CSIRO Marine Research, 53 2003.

NAKATO, T.; LOCHER, F. A.; GLOVER, J. R. and KENNEDY, J. F.: Wave entrainment of sediment from rippled beds. In: ASCE, J. of Waterway, Port, Coastal and Ocean Engineering, Vol. 103, 83–99, 1977.

NIELSEN, P.: Some basic concepts of wave sediment transport. Series Paper No. 20, Institute of Hydrodynamics and Hydraulic Engineering. Technical University of Denmark, 1979.

NIELSEN, P.: Suspended sediment concentrations under waves. In: Coastal Engineering, Vol.10, 23–31, 1986.

NIELSEN, P.: Dynamics and geometry of wave-generated ripples. In: J. of Geophysical Research, Vol. 86 (C7), 6467–6468, 1981.

NIELSEN, P.: Field measurements of time-averaged suspended sediment concentrations under waves. In: Coastal Engineering, Vol. 8, 51–72, 1984.

NIELSEN, P.: Coastal bottom boundary layers and sediment transport. Advanced series on Coastal Engineering, Vol. 4, World Scientific, 1992.

O'DONOGHUE, T. and CLUBB, G. S.: Sand ripples generated by regular oscillatory flow. In: Coastal engineering, Vol. 44, 101–115, 2001.

ONISHCHENKO, E. L. and KOS'YAN, R. D.: About use of optical method of determination of suspended sediment concentration in natural basins. In: Vodnye resursy (Water resources), № 3., 94-101, 1989.

OSBORNE, P. D.; VINCENT, C. E. and GREENWOOD, B.: Measurement of suspended sand concentrations in the nearshore: field intercomparison of optical and acoustic backscatter sensors. In: Continental Shelf Research, Vol. 14, No. 2/3, 159–174, 1994.

RIBBERINK, J. S.: Influence of wave-asymmetry and wave-irregularity on time- and bed-averaged sediment concentrations. In: Note H186.00-1 Delft Hydraulics, The Netherlands, 1987.

RIBBERINK, J. S. and AL-SALEM, A. A.: Sheet flow and suspension of sand in oscillatory boundary layers. In: Coastal Engineering, Vol. 25, 205-225, 1995.

RIBBERINK, J. S. and AL-SALEM, A. A.: Sediment transport in oscillatory boundary layers in cases of rippled beds and sheet flow. In: J. of Geophysical Research, Vol. 99(C6), 12,707–12,727, 1994.

ROLAND, P. J.: Using acoustic backscatter to measure sediment flux in the surf zone. Thesis. NAVAL postgraduate school, Monterey, California, USA, 2006.

SOULSBY, R.: Dynamics of marine sands. R. L. Soulsby and Thomas Telford Services Limited, UK, 1997.

SVENDSEN, Ib. A.: A model of sediment motion under waves. Internal Research Note, Technical University of Denmark, Inst. of Hydrodynamics and Hydraulic Engineering, 1977.

SVENDSEN, Ib. A.: Introduction to nearshore hydrodynamics. Advanced Series on Ocean Engineering, World Scientific, 2006.

THORNE, P. D; AGRAWAL, Y. C. and CACCHIONE, D. A.: A comparison of near-bed acoustic backscatter and laser diffraction measurements of suspended Sediments", In: IEEE, J. of Oceanic Engineering, Vol. 32, No. 1, 225–235, 2007.

THORNE, P. D and CAMPBELL, S. C.: Backscattering by a suspension of spheres. In: J. of the Acoustic Society of America, Vol. 92 (2), Pt 1, 978–986, 1992.

THORNE, P. D.; DAVIES, A. G. and WILLIAMS, J. J.: Measurements of near-bed intra-wave sediment entrainment above vortex ripples. In: J. of Geophysical Research, Lett., Vol. 30, No. 20, 2028, OCE, 2-1 - 2-4, 2003a.

THORNE, P. D., DAVIES, A. G. and WILLIAMS, J. J.: Measurements of intra-wave sediment entrainment over a rippled bed. In: ASCE, Proc. Coastal Sediments'03, in Clearwater, Florida, USA, 18- 23, 2003b.

THORNE, P. D.; DAVIES, A. G. and BELL, P. S.: Observations and analysis of sediment diffusivity profiles over sandy rippled beds under waves. In: J. of Geotechnical Research C02023, Vol. 114, 1-16, 2009.

THORNE, P. D. and HANES, D. M.: A review of acoustic measurement of small-scale sediment processes. In: Continental Shelf Research Vol. 22, 603–632, 2002.

THORNE, P. D. and HARDCASTLE, P. J.: Acoustic measurements of suspended sediments in turbulent currents and comparison with in-situ samples. In: J. of Acoust. Soc. Am., Vol. 101 (5), 2603–2614, 1997.

THORNE, P. D.; HARDCASTLE, P. J. and SOULSBY, R. L: Analysis of acoustic measurements of suspended sediments. In: J. of Geophysical Research (Oceans), Vol. 88 (C1), 899–910, 1993a.

THORNE, P. D.; MANLEY, C. and BRIMELOW, J.: Measurements of the form function and total scattering cross Section for a suspension of spheres. In: J. of Acoust. Soc. Am., Vol. 93 (1), 243–248, 1993b.

THORNE, P. D.; WILLIAMS, J. J. and DAVIES, A. G.: Suspended sediments under waves measured in a large-scale flume facility. In: J. of Geophysical Research (Oceans), Vol. 107, No. C8, 4.1-4.16, 2002.

THORNE, P. D.; WATERS, K. R. and BRUDNER, T. J: Acoustic measurements of scattering by objects of irregular shape. In: J. of Acoust. Soc. Am. Vol. 97 (1), 242–251, 1995.

PETERS, K. U. F.: Morphodynamik in der Brandungszone sandiger Küsten (Konzentrationsverteilung suspendierter, TU Braunschweig, Leichtweiß-Institut für Wasserbau (Herausgeber), Mitteilungen Heft 146, 166-411, 2000.

VAN DER WERF, J. J.: Sand transport over rippled beds in oscillatory flow. PhD thesis,University of Twente, The Netherlands, 2006.

VAN RIJN, L. C.: Manual sediment transport measurements. Delft Hydraulics Laboratory, Delft, The Netherlands, 1986.

VAN RIJN, L. C: Handbook: sediment transport by currents and waves. Delft Hydraulics, The Netherlands, 1989.

VAN RIJN, L. C.: Principles of sediment transport in rivers. Estuaries and coastal seas, Aqua Publications, Amsterdam, The Netherlands, 1993.

VAN RIJN, L. C.: Manual sediment transport measurements in rivers, estuaries and coastal seas. Aqua Publications, The Netherlands, 2006.

VINCENT, C. E and GREEN, M. O: Patterns of suspended sand. In: Soulsby, R. and Bettess Editors, Sand Transport in Rivers, Estuaries and the Sea. A.A. Balkema, Rotterdam, 117–124. 1991.

VINCENT, C. E and GREEN, M. O: The control of resuspension over megaripples on the continental shelf. In: ASCE, Proc. of Coastal Sediments'99, Long Island, USA, 269–280, 1999.

VINCENT, C. E. and OSBORNE, P. D.: Bedform dimensions and migration rates under shoaling and breaking waves. In: Continental Shelf Research, Vol. 13 (11), 1267–1280, 1993.

WIBERG, P. L. and HARRIS, C. K.: Ripple geometry in wave dominated environments. In: J. of Geophysical Research, Vol. 99 (C1), 775–789, 1994.

ZYSERMAN, J. A. and FREDSØE, J.: Data analysis of bed concentration of suspended sediment. In: J. of Hydraul. Engineering, Vol. 120 (9), 1021–1042, 1994.